Comparative study of three H2 geological storages in deep aquifers simulated in high-pressure reactors

Jean Mura, Magali Ranchou-Peyruse, Marion Guignard, Perla G Haddad, Marion Ducousso, Franck Casteran, Pascale Sénéchal, Marie Larregieu, M.-P. Isaure, Peter Moonen, et al.

International Journal of Hydrogen Energy 63 (2024) 330–345

Contents lists available at ScienceDirect

International Journal of Hydrogen Energy

journal homepage: www.elsevier.com/locate/he

Comparative study of three H_2 geological storages in deep aquifers simulated in high-pressure reactors

Jean Mura [a], Magali Ranchou-Peyruse [a,b,c], Marion Guignard [b], Perla G. Haddad [a], Marion Ducousso [a,c], Franck Casteran [a,c], Pascale Sénéchal [d], Marie Larregieu [b], Marie-Pierre Isaure [b], Peter Moonen [d], Isabelle Le Hécho [b,c], Guilhem Hoareau [e], Alice Baldy [b], Antoine Lafont [b], Anélia Petit [f], Pierre Chiquet [c,g], Guilhem Caumette [c,h], Pierre Cézac [a,c], Anthony Ranchou-Peyruse [b,c,*]

[a] Universite de Pau et des Pays de l'Adour, E2S UPPA, LaTEP, Pau, France
[b] Universite de Pau et des Pays de l'Adour, E2S UPPA, CNRS, IPREM, Pau, France
[c] Joint Laboratory SEnGA, UPPA-E2S-Teréga, Pau, France
[d] Universite de Pau et des Pays de l'Adour, E2S UPPA, CNRS, DMEX, Pau, France
[e] Universite de Pau et des Pays de l'Adour, E2S UPPA, CNRS, TOTAL, LFCR, Pau, France
[f] STORENGY – Geosciences Department, Bois-Colombes, France
[g] Teréga – Geosciences Department, Pau, France
[h] Teréga – Environment Department, Pau, France

ARTICLE INFO

Handling Editor: Dr. M. Djukic

Keywords:
Deep aquifers
Hydrogen
Deep subsurface
High pressure
UGS
UHS
Geological storage

ABSTRACT

Massive storage of dihydrogen (H_2) in underground geological storage (UGSs) will be necessary to meet future H_2 production ambitions. Such storage in deep aquifers was simulated in a high-pressure reactor, and the evolution of the 3 phases (natural gas/H_2, formation water and rock) with autochthonous microorganisms was monitored over several weeks. These results show that methanogens do not necessarily dominate the community, but that sulfate-reducing activity and formate bioproduction are systematically present. The experimental data were fed into a biochemical model in PHREEQC to better understand the interplay between the phenomena observed. In particular, it was shown that the microbial activities associated with H_2 consumption led to alkalinisation, which could explain, at least in part, the slower rate at which H_2 disappeared, even if sufficient CO_2 and sulfate remained in the system. Combined with a supposed local nutrient depletion, these results are encouraging for H_2 storage in deep aquifers.

1. Introduction

A global endeavor toward reducing fossil energy consumption is needed to combat global warming and resource depletion. Today, most energy production worldwide relies on fossil fuels [1]. Renewable energies can be a solution to resource depletion and greenhouse gas emissions [2–5]. However, most renewable energy sources are intermittent and do not necessarily match the production demand. Thus, an important challenge of renewable energy development and globalization is to transform and store the energy produced during periods of low demand. To promote the development of intermittent renewable energies (solar, wind), one considers injecting green dihydrogen (H_2) produced by electrolysis (Power-to-Gas) into the natural gas network. Indeed, power-to-gas could remediate the intermittency of renewable energies by using surplus electricity in periods of low demand [6]. To develop the H_2 sector, massive storage is needed under safe conditions. Underground gas storage (UGS) has been mastered for many decades and would enable large volumes of H_2 to be stored, particularly in deep aquifers. However, these environments are complex and need more research to evaluate the impact of H_2 storage.

H_2 storage in future underground hydrogen storage (UHS) raises the question of its behavior and stability, as it is a potentially reactive molecule. Indeed, H_2 is used as an electron donor and an energy source by autochthonous lithoautotrophic microorganisms [7–9]. Notably, H_2

* Corresponding author. Universite de Pau et des Pays de l'Adour, E2S UPPA, CNRS, IPREM, Pau, France.
E-mail address: anthony.ranchou-peyruse@univ-pau.fr (A. Ranchou-Peyruse).

https://doi.org/10.1016/j.ijhydene.2024.02.322
Received 6 October 2023; Received in revised form 31 January 2024; Accepted 25 February 2024
Available online 19 March 2024

is consumed by sulfate reducers and methanogens to reduce sulfate to sulfide and CO_2 to CH_4, respectively [10]. Acetate and formate can also be expected via the (homo)-acetogenesis pathway [9,11]. Additionally, microbial growth could lead to pore clogging by developing biofilms. The changes brought to the formation water by biological reactions could indirectly affect the porous rock by equilibrium displacement [12]. For example, bioalkalinization leads to the precipitation of carbonated minerals, and sulfate consumption leads to the dissolution of barite [13,14] with porosity and permeability changes. The injection of H_2 and its effects were shown to impact rock surface wettability in porous media [15–20]. Identifying and quantifying these reactions is key in assessing the UHS viability. Reviews suggest that microbial hydrogenotrophic activity represents a risk for the UHS and differs depending on the studied site [8,21,22] and recently, microbial activity under UGS was shown to be sulfate dependent [23]. As formation water and rock compositions are site dependent, site-specific studies are needed to determine the feasibility of H_2 storage.

The impact of H_2 on future UHS was estimated from town gas (16–60% H_2) storage in deep aquifers. Town gas was stored in the aquifers of Beynes (France), Lobodice (Czechia), and Ketzin (Germany) [8,24]. In the case of Lobodice, 45–60% of H_2 was reported to be converted to methane and hydrogen sulfide after seven months of storage [7]. In Beyne storage, strong microbial activity was reported, but H_2 consumption was not studied [8]. However, abiotic production of sulfide attributed to pyrite reduction has been discussed [25]. In Ketzin, the active microbial processes were not clearly identified, but the consumption of carbon monoxide and production of CO_2, H_2, and CH_4 were documented [8,26]. The behavior of the UGS observed in these three documented cases shows large differences between storages [27].

Recently, multiple large-scale UHS experiments have been conducted or are under investigation worldwide [8,28]. However, these experiments are mainly conducted in salt caverns. Depleted gas reservoirs and deep aquifer H_2 storage experiences remain largely limited to past town gas storage (Table 1). To fill the knowledge gap of H_2 storage in porous media, the SUN [29], HyUSPRe [30], and Hystories [31] projects are currently being conducted and aim to provide technical development and techno-economical evaluation of the feasibility of this kind of storage in depleted reservoirs. Recently, kinetics modeling studies were performed to evaluate the impact of H_2 storage in the presence of hydrogenotrophic microorganisms [32–35]. All studies showed H_2 consumption and impact on pH and pointed out the need for more experimental studies to upscale the models to the storage scale. There are still doubts about the nature of the cushion gas, and even if there will be one. In situ H_2 storage experiments (in the presence of town gas or methane) have all shown hydrogenotrophic microbial activity. CO_2 as a cushion gas remains a possibility only tested in numerical simulation, although analogues exist in some hydrocarbon reservoirs treated with CO_2-EOR.

In this study, we present two experiments of H_2 storage simulated in a high-pressure reactor on two different Parisian aquifers (Pb_J_11 and Pb_C_5) used as UGS to store methane. It makes sens to be interested in these systems, since it is obvious that future UHS will mainly be built in existing UGS for economic reasons, and it seems likely that cushion gases in UHS could be composed of methane, which would interact with the stored H_2 [36]. Firstly, the results are presented and compared to a previously published study on another site (Pb_T_1) using the same experimental protocol [9]. The reactor contained formation water with autochthonous microorganisms and rock samples from the studied aquifers. A gas phase representing currently stored natural gas was initially injected, and different proportion of H_2 were added. Multidisciplinary analyses were performed before, during, and after the experiments to characterize the gaseous, liquid and solid phases. Next, *in situ* thermodynamic modeling was performed, and the extents of the reaction equations were solved to better correlate and identify the intricate phenomena observed. This is followed by a discussion of these results closely linked to the microbial metabolisms, as well as to the physico-chemical and mineralogical evolution of the solid, liquid and gaseous phases. Finally, the findings are highlighted with regards to the future use of UHS.

2. Materials and methods

2.1. Simulated sites and sample characteristics

All three experiments were carried out to simulate targeted aquifers used for UGS. Being sampled from monitoring wells close to the gas–liquid interface, formation waters were greatly exposed to the stored natural gas. Each formation water was sampled from the studied aquifer

Table 1
Examples of studies on hydrogen storage in porous reservoirs (aquifer and depleted reservoir), taking into account microorganisms.

Type of storage	Cushion gas	Study	Microorganisms identified or studied	Microbial products	Amount of products	H_2 losses (%)	References
Aquifer	town gas	*in situ*	methanogens and sulfate-reducers supposed	CH_4	an increase of 45% of CH_4	60–70%	[7,25,37]
Aquifer	CH_4	*in situ*	at that time, the microorganism track had been put aside	CH_4, H_2S	an increase of CH_4 and H_2S (2–40 ppm)	N/A	[38–40]
Depleted reservoir	CH_4	*in situ*	methanogens and sulfate reducers	CH_4, H_2S	CH_4, H_2S not detected	18%	[29,34]
Depleted reservoir	CH_4	*in situ*	No gas composition results published				[41,42]
Ketzin	town gas	*in situ*	microbial activity suspected	N/A	H_2S	61%	[26,43]
Aquifer	CH_4	HP reactor	methanogens, acetogens and sulfate-reducers	CH_4, H_2S, formate	not determined	40%	[9]
Depleted reservoir	CH_4	HP reactor	few methanogens, no sulfate reducers	No significant microbial activities			[44]
Depleted reservoir	CH_4	HP reactor	sulfate-reducers; no methanogens	H_2S	500 µmol	4088 µmol/day L	[23]
Aquifer	town gas	numerical modeling	methanogens, acetogens and sulfate-reducers	CH_4, H_2S	an increase of 65% of CH_4, 0,07% H_2S	complete	[32]
Depleted reservoir	CO_2	numerical modeling	methanogens, sulfate-reducers	assumed limited	assumed limited	<2%	[45]
Depleted reservoir	CH_4	numerical modeling	methanogens, sulfate-reducers	assumed limited	assumed limited	assumed <0,1%	[46]
Depleted reservoir	CH_4/CO_2	numerical modeling	methanogens, sulfate-reducers, acetogens, iron-reducers	CH_4, Acetate, H_2S, Fe_3O_4	not determined	not determined	[47]
Depleted reservoir	CH_4	numerical modeling	methanogens	CH_4	not determined	21%	[48]

using a protocol guarantying the preservation of autochthonous microorganisms and the lack external contamination using a downhole sampler (Leutert Bottom Hole Positive Displacement Sampler) [9,49,50]. The characteristics, water compositions, and sampled volumes of the three studied sites are summarized in Table 2. The pressure and temperature of the reactor were fixed and set to the aquifer's conditions for each experiment and ranged from 85 to 95 bar and 35–47 °C depending on the studied site. The solid phase was recovered from drillings in the formation rock of the studied aquifers. Rocks were crushed, with the exception of a small core (approx. 3 cm long and 7 mm in diameter) for X-ray tomography. As a reminder, the water from the first site studied (Pb_T_1) [9] had low salinity and the lowest sulfate concentration of the three experiments discussed in this study. At this site, the rock is mostly composed of sandstone and calcite. Effects of a single injection of 10% H_2 in the gas phase of the high-pressure reactor were studied after 21 days of incubation. Results from this experiment were described in a previous study [9] and were compared with two new experiment carried in this work. The second site was previously studied in the literature [40] in the context of natural gas storage and was referred to as Pb_J_11. For this experiment, water was sampled from a Sequanian aquifer (836 m deep). The rock is mostly composed of quartz and clays. A single injection of 9% H_2 was performed after 43 days of incubation. The third site, coded Pb_C_5, was a Hauterivian aquifer (840 m deep). The rock at this site is still mostly composed of quartz and clays. In this experiment, the setpoint for the H_2 molar percentage was 2%. After the initial injection (day 36), when the H_2 concentration dropped below 1%, additional injections were provided to bring the H_2 percentage back to 2% (days 64 and 107).

2.2. Solid phase preparation

Solid phases were rinsed with isopropanol and ultra-pure water to remove potential residual hydrocarbons, drilling salts, and microorganisms. Afterward, the solids were dried in an oven at 90 °C overnight.

Table 2
Characteristics and composition of the formation waters sampled from the studied UGS aquifers. Analyses were carried out at atmospheric pressure.

Parameters		Value		Unit
Site characteristics				
Site	Pb_T_1	Pb_J_11	Pb_C_5	
Depth	989	836	840	m
Geological formation	Triassic	Sequanian	Neocomian	
Pressure	95	85	85	Bar
Temperature	47	35	41	°C
pH	7.9	8.0	8.5	
Redox Potential	−365.6	−298.6	−178	mV
Conductivity at 25 °C	1.2	6.5	6.2	mS/cm
Organic Carbon	<1	<1	<1	mg/L
Water composition				
Chloride	7.1	11.62	8.04	mM
Nitrate	<0.0016	<0.0016	<0.0016	mM
Nitrite	<0.0004	<0.02	<0.02	mM
Sulfate	0.15	13.03	25.06	mM
Carbonate	<1	<1	<1	mM
Bicarbonate	8.51	34.45	12.31	mM
Calcium	0.26	1.24	0.63	mM
Ferrous iron	<0.89	0.08	0.21	µM
Total iron	6.88		0.40	µM
Magnesium	0.14	1.57	0.83	mM
Potassium	0.27	0.65	0.82	mM
Sodium	14.89	62.782	65.35	mM
Water volumes				
Formation water	1.088	1.162	1.176	L
0.1 µm filtered - wellhead water	0.612	0.788	0.774	L
Water available after analyses	1.460	1.702	1.690	L

2.3. Experiments

2.3.1. The three-phase high-pressure reactor

Experiments were carried out in a high-pressure (HP) reactor (Figure S1) made of Hastelloy C-276, which can be operated up to 150 bars and 150 °C [9,49]. It is equipped with two thermocouples to monitor the temperature of the liquid and gas phases. The pressure evolution was monitored by a Keller PA(A)-33× pressure gauge with 0.3 bar precision. The solid phase was contained in a 225 mL Teflon basket placed in the middle of the reactor, permitting contact of both gaseous and liquid phases with the rock. The bottom of the basket is a Hastelloy C-276 disc with 10 µm pores. The volume of the reactor is rendered variable by a moving piston, allowing to maintain the water constant despite liquid samplings. The liquid and gaseous phases were stirred at 20 rpm by a Rushton turbine and a double disc stirrer with four vertical blades, respectively.

2.3.2. Experimental protocol

Before injecting the formation water and the gas phases, the HP reactor was sterilized at 110 °C for 24 h [49]. The liquid phase containing microorganisms was injected into the HP reactor from an N_2 inert Teflon bottle. The height of the piston was set to fully immerse the solid phase and allow optimal contact with liquid phase. The initial gas mix injected was composed of 99% CH_4, 1% CO_2, 7.95 ppm of benzene, and 3.57 ppm of toluene (BT) to simulate a natural gas. This gas mix was injected at 1 bar min^{-1} until reaching the pressure setpoint. After seven days, the piston was lowered to have the liquid-gas interface in the rock phase as in UGS (1 cm of submerged rock). The associated pressure drop was compensated by injecting the initial gas mix. After validation of the microbial activity, H_2 (purity 99.999%) was injected to reach the desired set point. During the experiments, liquid and gas phase analyses were carried out weekly, and additional analyses were performed on specific occasions. Pressure drops were automatically compensated by moving the piston to maintain a constant pressure throughout the experiment. After opening the reactor, the solid basket was quickly and cautiously removed and placed into an inerted box containing an anaerobiosis generator and indicator pockets (Dutscher Ref 0260001). Rocks were then processed in an anaerobic glove box (Jacomex) to prepare the analyses for the solids. The work procedure is summarized in a flowchart (Figure S2).

2.3.3. Physico-chemical analyses

From the liquid phase, fluoride, acetate, formate, chloride, and sulfate were monitored by anionic chromatography (Dionex Integrion HPIC, ThermoFisher Scientific) with ±5% precision. Sodium, potassium, magnesium, and calcium were followed by cationic chromatography (ICS-900, Dionex) with ±5% precision. Inlab Ultramicro ISM (Mettler Toledo) and Inlab Redox Micro (Mettler Toledo) electrodes were used to monitor the pH and the oxidation–reduction (redox) potential of the samples, respectively. The gas phase was analyzed (CH_4, CO_2, H_2, H_2S) in line using gas chromatography with a microthermal conductivity detector (GC-mTCD; Micro GC Fusion; Chemlys; France). The measurement uncertainty was ±5%, and the analyses were performed in triplicate.

The CSIA (Compounds Specific Isotope Analysis) approach was performed using an analytical chain composed of a gas chromatograph (GC, Thermo, Trace 1310) coupled, via a combustion interface at 1000 °C (CT, Thermo, GC-Isolink), to an isotope ratio mass spectrometer (IRMS, Thermo Delta V Plus) to estimate a possible natural *in situ* bioattenuation [51,52]. In parallel, the identification and quantification of benzene and toluene (BT) in the liquid and gas phases were carried out by coupling gas chromatography to a quadrupole mass spectrometer (MS, Thermo, ISQ). Physicochemical analysis protocols were detailed in the work of Haddad et al., 2022 [49].

2.3.4. Molecular biology approaches

Molecular biology protocols were carried out as described in Ref. [49] to compare the results of all studies that have been conducted with this HP reactor. Briefly, water samples (70 mL) were collected at key periods of the experiments (transition time) and filtered on PES membrane filters (47 mm, 0.1 μm porosity, Sartorius Stedim). The filters were stored at −80 °C until use. Nucleic acid extractions were performed with the Fast RNA ProSoil Direct Kit (MPBio) after a filter grinding step in liquid nitrogen. DNA was then separated from RNA using the All Prep RNA/DNA kit (Qiagen). RNA was reverse transcribed into cDNA using M-MLV reverse transcriptase (Invitrogen™). The V4–V5 region of the *16S rRNA* gene of each extracted DNA and cDNA was amplified. Illumina sequencing was performed by the GenoToul genomics platform (Toulouse, France) using Illumina's MiSeq 2 × 250 bp technology. Raw sequencing data for Pb_T_1, Pb_J_11 and Pb_C_5 were deposited in the NCBI SRA under bioprojects ID PRJNA813384, PRJNA1023401 and PRJNA1023500, respectively. The sets of sequences from the 3 experiments [9], and two from this study, were processed using QIIME2-2021.4 [53]. with DADA2 [54] with singleton removal. Taxonomic assignment was performed using the SILVA 138 database. *16S rRNA* copies of transcripts and genes (all prokaryotes), *dsrB* (sulfate reducers) and *mcrA* (methanogenic archaea) were quantified by qPCR and RT−qPCR as previously described [9].

2.3.5. X-ray computed tomography

The morphological alterations of the solid phase were followed by X-ray computed tomography during the experiments on Pb_J_11 and Pb_C_5. Teflon tubing with an internal diameter of 7 mm and a height of 3 cm was filled with cylinders of consolidated rock. Before the experiment, samples were scanned for initial reference and placed vertically in the basket with the remaining rock. After the completion of the experiment, the samples were removed and hermetically sealed at both ends in an anaerobic glove box (Jacomex) with waterproof glue and stored at 4 °C until scanning. The scans were performed with Zeiss Xradia versa 510 (Pb_J_11 scans and Pb_C_5 reference scans) and Tescan UnitomXL (Pb_C_5 final scans) tomographs and analyzed with Dragonfly (ORS) software.

2.3.6. X-ray diffraction

The solid phases were characterized by X-ray diffraction (XRD) before and after the two experiments to detect potential variation in the mineralogical composition induced by precipitation and/or dissolution. At the end of the experiment, samples were collected from the basket at three different depths in the anaerobic glove box. Samples were dried with N_2 gas flux to limit oxidation, manually ground and sieved <100 μm into a homogeneous powder in a N_2 atmosphere. Solid powders were then mounted on holders and directly analyzed by XRD. The analyses were performed using a Bruker D2 Phaser powder diffractometer equipped with a Cu Kα radiation source. XRD patterns were recorded over a 5°–90° 2Θ range with a 0.02° step and a 0.5 s counting time per step. DIFFRAC. EVA software was used to identify and quantify the mineral phases.

2.3.7. Scanning electron microscopy with energy dispersive X-ray (SEM/EDX)

SEM/EDX was used to localize and identify mineral phases in the Pb_J_11 experiment. Samples collected at the three depths of the reactor in the glove box were kept at 4 °C. Samples were then mounted on stubs, plunged in liquid nitrogen and cryo-fractured just before the observation. They were sublimated at −80 °C and metallized with platinum. Measurements were taken with a SEM Gemini Zeiss 300 combined with energy dispersive analysis (EDX, Gatan) in cryogenic mode. Analyses were performed at 8 kV in secondary electron mode. For the Pb_C_5 experiment, the samples, carbon-coated and mounted on stubs, were observed using an SEM-FEG JEOL JSM 7800F Prime equipped with an SDD X-Max 80 mm^2 energy-dispersive X-ray spectrometer (EDS; Oxford Instruments AZtecEnergy) at the Centre Castaing, Toulouse, France.

2.3.8. Biochemical modeling

2.3.8.1. Thermodynamic in situ modeling. The gas−liquid interaction in the HP reactor was modeled using the widely used geochemical software PHREEQC [55]. The primary purpose of this modeling approach was to estimate gas solubility, which significantly influences pH and redox potential [56]. For each key experiment point (injection or disappearance of compounds), the thermodynamic equilibrium between the liquid and gas phases was modeled, considering them homogenous (0D model). This calculation enabled us to estimate gas solubility and the resulting pH and redox potential during the experiment. The database phreeqc. dat was used to model the liquid-vapor equilibrium. The nonideality of the gas phase was considered using the Peng-Robinson equation of state [57], allowing us to compute gas solubility at high pressure. This modeling was performed at steady state, assuming equilibrium for each simulation. Slow redox reactions were removed from the database to represent redox disequilibrium [32]. The redox potential calculation was based on the Nernst potential of the sulfate/sulfide, H^+/H_2, and CO_2/CH_4 couples (Eqs. (A.1)–(A.3)) using phreeqc. dat parameters [58–60]. The model setup is developed in Appendix A.

2.3.8.2. Extent of reaction equations based on microbial diversities. The extent of reaction equations based on microbial diversity was solved to identify and estimate microbial reactions. Four reactions were selected based on the microbial diversity results (Fig. 1). It was assumed that all mechanisms were hydrogenotrophic: methanogenesis [61–63], sulfate reduction [25,62,64], acetogenesis [65,66], and formate production [67]. The extent of each mechanism's reaction was calculated based on the evolution of a selected component. In that regard, CO_2, sulfate, acetate, and formate quantity evolutions were used to determine the extent of the methanogenesis, sulfate reduction, acetogenesis, and formate production reactions, respectively. For gas species, the dissolved quantity in all protonation states was considered using the previous solubility calculations. The quantity of matter of gas species was calculated by the Peng-Robinson EOS based on the gas phase analyses and the volume, pressure, and temperature of the reactor. The speciation of H_2S was considered based on the *in situ* modeling conducted previously, as it influences the consumption of H_2 ions by sulfate reduction (Eq. (2)). The stoichiometry of H_2S in Eq. (2) (liquid and gaseous) noted ν is indicated for each experiment. Acido-basic buffering attributed to the $CO_2/\ HCO_3^-$ couple was considered (Eqs. (1)–(4)).

$$CO_2 + 4H_2 \rightarrow\ CH_4 + 2H_2 \quad \text{Eq. (1)}$$

$$SO_4^{2-} + 4H_2 + (1+\nu)\ CO_2 \rightarrow (1-\nu)HS^- + \nu H_2S + (1+\nu)HCO_3^- + (3-\nu)H_2O \quad \text{Eq. (2)}$$

$$CO_2 + HCO_3^- + 4H_2 \rightarrow AcO^- + 2H_2O \quad \text{Eq. (3)}$$

$$HCO_3^- + H_2\ \rightarrow HCOO^- + H_2O \quad \text{Eq. (4)}$$

The solved system is represented by equations B.1 to B.8 (Appendix B).

3. Results

3.1. Physicochemical monitoring of the gas phase evolution during the experiments

3.1.1. Pb_J_11, samples from a sedimentary layer dated Jurassic (836 m deep)

Initially, 80.1 ± 0.3 bar of the CH_4 + 1% CO_2 + BT gas mix was injected into the reactor at 36 ± 1 °C. Thus, initially, 5.72 ± 2.1 × 10^{-2} mol of CH_4 and 5.78 × 10^{-2} ± 2.2 × 10^{-4} mol of CO_2 (Fig. 2 A2) were

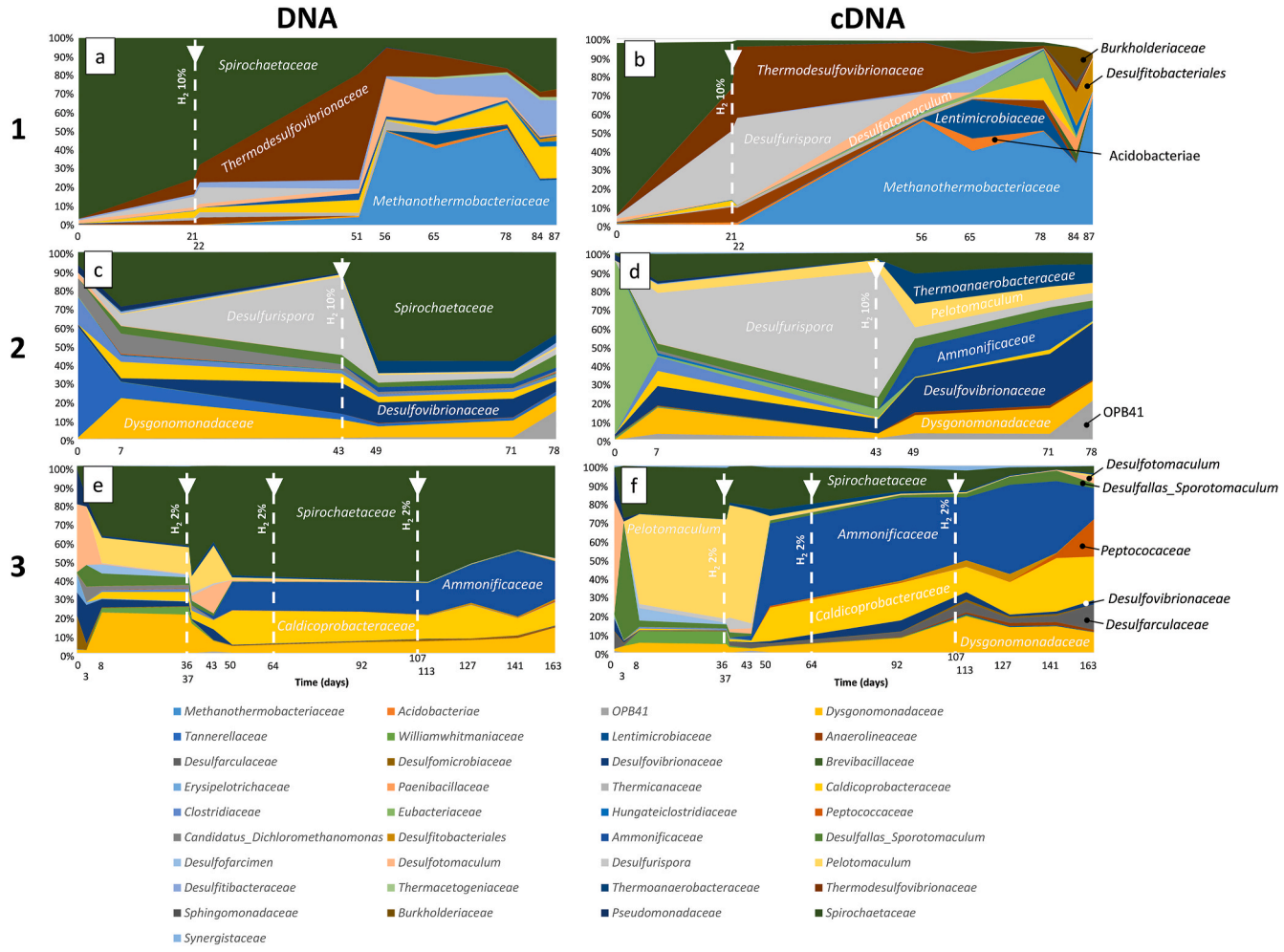

Fig. 1. Relative abundance of the taxonomic diversity of microbial communities from three deep aquifers. Each experiment was conducted in a high-pressure reactor with a gas phase composed of CH_4 and 1% CO_2 and with injections of H_2. The processed data are from high-throughput sequencing performed on the *16S rRNA* genes (left column) and transcripts (right column). 1) Samples from site Pb_T_1 (989 m depth; data from Haddad et al., 2022) with incubation at 47 °C and 85 bar with 10% H_2 injection on day 21 (a and b). 2) Samples from site Pb_J_11 (836 m depth; data from this study) with incubation at 35 °C and 85 bar with an injection of 9% H_2 on day 43 (c and d). 3) Samples from site Pb_C_5 (840 m depth; data from this study) with incubation at 41 °C and 85 bar with an injection of approximately 2% H_2 on days 36, 64 and 107 (e and f).

injected. A loss of $1.8 \times 10^{-2} \pm 2.1 \times 10^{-3}$ mol of CO_2 was observed on day 7 after gas solubilization into the formation water (Fig. 2 B1). Next, the piston was lowered to immerse only 1 cm of solid. Consequently, the initial CH_4/1% CO_2/BT gas mix was injected to compensate for the pressure drop from the piston descent. This injection added $5.34 \times 10^{-1} \pm 2.0 \times 10^{-3}$ mol of CH_4 and $5.39 \times 10^{-3} \pm 2.0 \times 10^{-5}$ mol of CO_2 in the reactor. No significant variation in the CH_4 quantity was observed during the experiment. The CO_2 quantity was stable before the H_2 injection. Between H_2 injection and the end of experiment, $2.1 \times 10^{-2} \pm 2.2 \times 10^{-3}$ mol of CO_2 were consumed. At the end of the experiment, $2.3 \times 10^{-2} \pm 1.1 \times 10^{-3}$ mol of CO_2 remained in the gas phase. H_2 was injected on day 43, resulting in a molar percentage of 8.9 ± 0.4%. The quantity of H_2 injected was $5.91 \times 10^{-1} \pm 2.2 \times 10^{-3}$ mol (Fig. 2 A2). The solubility of H_2 was low, and no significant drop in H_2 quantity was observed directly after injection. The amount of H_2 decreased by $8.8 \times 10^{-2} \pm 2.9 \times 10^{-3}$ mol from day 43 to the end of the experiment. At the end of the experiment, $5.02 \times 10^{-1} \pm 2.5 \times 10^{-3}$ mol of H_2 remained in the gas phase, and the final H_2 percentage was 7.7 ± 0.4%. H_2S was detected in the gas phase on day 46, shortly after H_2 injection, and increased to a maximum of $2.7 \times 10^{-3} \pm 1.3 \times 10^{-4}$ mol on day 57. Then, the amount of H_2S decreased slightly until the end of the experiment ($2.4 \times 10^{-4} \pm 1.2 \times 10^{-4}$ mol on day 78).

3.1.2. *Pb_C_5, samples from a sedimentary layer dated early cretaceous (840 m deep)*

The initial gas mix was injected into the reactor at 83.85 ± 0.3 bar and 40 ± 1 °C. This injection introduced $6.15 \pm 2.2 \times 10^{-2}$ mol of CH_4 and $6.21 \times 10^{-2} \pm 2.2 \times 10^{-4}$ mol of CO_2 in the reactor (Fig. 2 A3). On day 7, after solubilization, a loss of $1.5 \times 10^{-2} \pm 3.1 \times 10^{-3}$ CO_2 moles was measured. On this day, the piston was lowered, and the gas mix was injected to counteract the pressure loss induced. This injection added $2.42 \times 10^{-2} \pm 8.5 \times 10^{-4}$ mol of CH_4 and $2.42 \times 10^{-3} \pm 3.1 \times 10^{-6}$ mol of CO_2 in the reactor. No significant variation in the CH_4 quantity was observed during the incubation. After the H_2 injection, CO_2 continuously decreased until the end of the experiment but was not completely depleted. On day 148, only $4.3 \times 10^{-3} \pm 2.1 \times 10^{-4}$ mol of CO_2 remained in the gas phase. H_2 injection on day 36 brought $1.29 \times 10^{-1} \pm 4.6 \times 10^{-4}$ mol into the reactor (Fig. 2 A3), resulting in a molar ratio of 1.63 ± 0.08%. To get closer to the 2% objective, $3.07 \times 10^{-2} \pm 1.1 \times 10^{-4}$ mol was injected on day 37. The H_2 percentage after the second injection was 1.90 ± 0.09%. H_2 decreased and reached $5.7 \times 10^{-2} \pm 5.8 \times 10^{-3}$ mol on day 64, resulting in the H_2 ratio decreasing to 0.92 ± 0.05%. On this day, $6.92 \times 10^{-2} \pm 2.5 \times 10^{-4}$ mol of H_2 was injected and brought its molar percentage up to 1.79 ± 0.09%. The H_2 decrease continued after reinjection, and on day 107, $5.6 \times 10^{-2} \pm 5.5 \times 10^{-3}$ mol was consumed, and the H_2 percentage reached 0.83 ± 0.04%. A

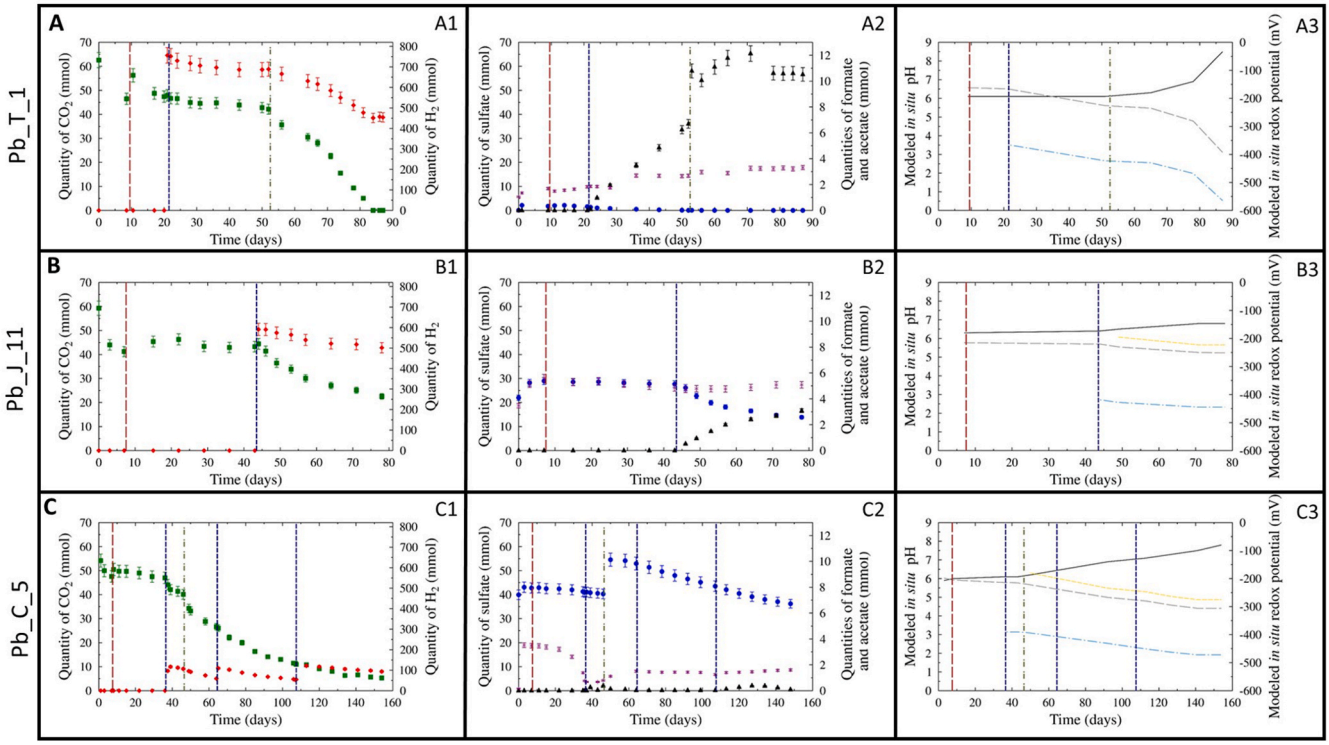

Fig. 2. Variations in physicochemical parameters in the aqueous phase and gas phase composition during the experiments. The brown, blue and green vertical lines correspond to the $CH_4 + CO_2$ reinjections, hydrogen injections and formation water reinjection, respectively. The left column (1) presents the gaseous phase with CO_2 (green squares) and H_2 quantity (red dots), the middle column (2) presents the liquid phase sulfate (blue dots), acetate (purple cross) and formate (black triangles) matter quantity and the right column (3) presents the modeled *in situ* pH (black curve) and redox potential. The yellow, gray and blue curves represent the carbon, sulfur and hydrogen Nernst redox potentials, respectively. A) Experiment at site Pb_T_1. (data from Haddad et al., 2022). B) Experiment on site Pb_J_11 (data from this study). C) Experiment on site Pb_C_5 (data from this study).

final injection of $7.94 \times 10^{-2} \pm 2.8 \times 10^{-4}$ mol of H_2 was performed on this day, bringing the H_2 percentage up to $2.07 \pm 0.1\%$. At the end of the experiment, $9.3 \times 10^{-2} \pm 4.7 \times 10^{-3}$ mol remained, and the H_2 percentage was $1.54 \pm 0.08\%$. From H_2S detection in the gas phase on day 46, its quantity increased to $1.97 \times 10^{-3} \pm 9.9 \times 10^{-5}$ mol on day 78. Then, H_2S decreased to a minimum of $4.1 \times 10^{-4} \pm 2.0 \times 10^{-5}$ mol on day 154.

3.2. Physicochemical monitoring of the liquid phase

3.2.1. Pb_J_11, samples from a sedimentary layer dated Jurassic (836 m deep)

The ionic composition of the formation water was mostly sodium (62.78 mM), bicarbonate (34.5 mM), sulfate (13.03 mM), and chloride (11.62 mM). Acetate (2.07 mM), calcium (1.24 mM), magnesium (1.57 mM), and potassium (0.65 mM) were also contained at lower concentrations. Sulfate had one of the highest initial quantities ($1.92 \times 10^{1} \pm 9.6 \times 10^{-1}$ mmol) of the present ions (Fig. 2 B2). After contact with the formation water with the solid phase, the sulfate quantity increased to $2.52 \times 10^{1} \pm 1.3$ mmol after 7 days. From day 7 to H_2 injection (day 43), a slight but perceptible sulfate decrease to $2.41 \times 10^{1} \pm 1.2$ mmol was observed. After H_2 injection, sulfate decreased to $1.26 \times 10^{1} \pm 6.3 \times 10^{-1}$ mmol at the end of the experiment. Calcium ions were initially contained in the liquid phase ($3.9 \pm 1.9 \times 10^{-1}$ mmol), and this quantity remained stable until the H_2 injection (day 43). From day 49 to the end of the experiment, the Ca^{2+} quantity decreased and bottomed at $2.4 \pm 1.2 \times 10^{-1}$ mmol. Formate (Fig. 2 B2) was not detected in the formation water initially injected into the reactor. Formate production was observed after H_2 injection, reaching $2.90 \pm 1.4 \times 10^{-1}$ mmol on day 78. Acetate (Fig. 2 B2) was initially contained in the formation water ($3.02 \pm 1.5 \times 10^{-1}$ mmol). The acetate quantity quickly increased to $4.88 \pm 2.4 \times 10^{-1}$ mmol on day 7. A decrease was observed until acetate reached $4.12 \pm 2.1 \times 10^{-1}$ mmol on day 46, just after H_2 injection. From day 46 to day 78, the quantity of acetate slightly increased to a maximum of $4.69 \pm 2.3 \times 10^{-1}$ mmol.

3.2.2. Pb_C_5, samples from a sedimentary layer dated early cretaceous (840 m deep)

The formation water was mostly composed of sodium (65.35 mM), sulfate (25.06 mM), bicarbonate (12.3 mM), and chloride (8.04 mM). Magnesium (0.83 mM), potassium (0.82 mM), calcium (0.63 mM), and acetate (0.09 mM) were also contained in the formation water at lower concentrations.

The sulfate (Fig. 2 B3) quantity was initially high ($3.99 \times 10^{1} \pm 2.0$ mmol). After interaction with the rock, the sulfate quantity increased to a maximum of $4.31 \times 10^{1} \pm 2.1$ mmol on day 3. The sulfate quantity decreased slowly until H_2 injection on day 36 ($4.09 \times 10^{1} \pm 2.0$ mmol). Between the first H_2 injection and the filter-sterilized formation water supplementation on day 46, sulfate continued to decrease slowly ($4.03 \times 10^{1} \pm 2.0$ mmol). This supplemented water compensated for the sampled used for analyses, allowing the duration of the experiment to be extended. The added volume of water increased the sulfate quantity to $6.13 \times 10^{1} \pm 3.1$ mmol. From day 50 to the end of the experiment on day 148, sulfate decreased faster and reached a minimum of $4.64 \times 10^{1} \pm 2.3$ mmol. Calcium and magnesium were present in low quantities ($8.9 \times 10^{-1} \pm 4.5 \times 10^{-2}$ mmol and $1.41 \pm 7.0 \times 10^{-2}$ mmol) in the initial formation water. On day 3, calcium and magnesium quantities both increased to the same value of $3.0 \pm 1.5 \times 10^{-1}$ mmol. Both quantities remained constant until the first H_2 injection (day 36). From day 42–45, the calcium quantity decreased to $1.84 \pm 9.2 \times 10^{-2}$ mmol and remained stable until the end of the experiment. From days 42–63, magnesium increased to $8.6 \pm 4.3 \times 10^{-1}$ mmol and then remained

stable until the end of the experiment.

Acetate (Fig. 2 B3) was initially present in low quantities ($1.56 \times 10^{-1} \pm 7.8 \times 10^{-3}$ mmol) in the formation water, whereas formate was not detected. After injection in the reactor, the acetate quantity quickly increased to a maximum of $3.53 \pm 1.8 \times 10^{-1}$ mmol on day 3. Then, the acetate quantity decreased until total consumption before the first H_2 injection (day 36). Formate appeared on day 39 after H_2 injection and reached a maximum quantity of $3.72 \times 10^{-1} \pm 1.9 \times 10^{-2}$ mmol on day 46. From day 46 to the third H_2 injection (day 64), acetate increased steadily ($1.50 \pm 7.5 \times 10^{-2}$ mmol), and formate decreased to total consumption. From the fourth injection (day 107) to day 148, acetate increased again but at a lower speed. At the end of the experiment, the acetate quantity was $1.60 \pm 8.0 \times 10^{-2}$ mmol. At that time, formate was detected again and increased to a maximum of $3.79 \times 10^{-1} \pm 1.9 \times 10^{-2}$ mmol on day 107 before decreasing to $8.28 \times 10^{-1} \pm 4.2 \times 10^{-3}$ mmol at the end of the experiment.

The results from the 3 experiments are summarized and compared in Table 3.

3.3. Benzene and toluene (BT) evolution

Monoaromatic hydrocarbons were added to the gaseous phase to achieve conditions similar to those in the field. The results obtained were similar for both pilots, as shown in Fig. 3. The measured amounts of BT followed the same trends. For the gas phase, considering the standard deviations, the values obtained for toluene were not significantly different. For benzene, the last two sampling points may have suggested the beginning of biodegradation (47.7% decrease between day 3 and day 78). The experiment did not last long enough to demonstrate this, as the degradation of benzene by sulfate reducers is slower than toluene degradation [68]. For the liquid phase in equilibrium with the gaseous phase, the measured quantities were constant during the experiment because of thermodynamic constraints [69]. However, the isotopic values obtained in the liquid and gas phases were relatively stable, considering the standard deviations. The conditions of the experiment (duration, H_2 additions) did not allow us to highlight the biodegradation of BT by the sole determination of the isotope ratios. The determination of the enrichment factors $\Delta\delta^{13}C$ of benzene and toluene estimated by the difference of the isotopic values between two phases (gas and water) were calculated from the determination of the carbon isotopic ratio of benzene and toluene in the liquid and gas phases. The calculated values of $\Delta\delta^{13}C$ for benzene are of the order of 1‰ (1‰ and 1.4‰ for the Pb_J_11 and Pb_C_5 experiments, respectively) and less than 0.1‰ for toluene (0.9‰ and 0.2‰ for the Pb_J_11 and Pb_C_5 experiments, respectively). The values therefore show that whatever the experiment considered, no enrichment in heavy carbon isotopes for benzene and toluene in water is evidenced. Determination of the isotope ratios in these experiments does not therefore show that there is bio-attenuation since biodegradation in the aqueous phase is considered to have been demonstrated when $\Delta^{13}C > 2‰$ [70].

Table 3
Comparison of the result from the three experiments of H_2 injection in the HP reactor simulating aquifers conditions.

Pb_T_1	Pb_J_11	Pb_C_5
Total sulfate consumption (0.81 mmol)	Partial sulfate consumption (10.3 mmol)	Partial sulfate consumption (14.9 mmol)
Total CO_2 consumption (47.8 mmol)	Partial CO_2 consumption (28.2 mmol mmol)	Partial CO_2 consumption (45.8 mmol)
High alkalinisation (pH 8.5)	Low alkalinisation (pH 6.8)	High alkalinisation (pH 7.8)
H_2S under detection limit	High H_2S quantity (9.2 mmol)	High H_2S quantity (18.9 mmol)
Restructuration of the microbial community.		
Low changes in porosity and mineralogy.		

3.4. Microbial community evolution during the experiments

The results shown in Fig. 1a and b were from a previous work on sampling site Pb_T_1 [9] and were presented in this paper for comparison with the two new experiments performed with samples from two other UGS of this study (Pb_J_11 and Pb_C_5). Briefly, in Pb_T_1, the microbial community was dominated on day 21 by fermenters with the family *Spirochaetaceae* (74%) and sulfate reducers belonging to the family *Thermodesulfovibrionaceae* and the spore-forming genus *Desulfurispora* (6%). The injection of 10% H_2 (day 21) led to a restructuring of the microbial community with an increase in *Thermodesulfovibrionaceae* and *Methanothermobacteriaceae* (hydrogenotrophic methanogens). From the 51st day and the complete depletion of sulfate, the family *Methanothermobacteriaceae* became dominant and represented up to 50% of the community on the 56th day, and some members of the genus *Desulfotomaculum* (20% on day 56) and of the families *Caldicoprobacteraceae* (17% on day 87) and *Desulfitibacteraceae* (18% on day 87) developed. The biological sample processing and high-throughput sequencing performed in the study presented here were performed identically to those obtained for Pb_T_1 [9]. The sequencing data from the three experiments were analyzed together, allowing for comparison. The number of sequences analyzed after cleaning for the Pb_J_11 (Fig. 1c and d) and Pb_C_5 (Fig. 1e et 1f) sites were 302,106 and 642,799, respectively.

3.4.1. Pb_J_11, samples from a sedimentary layer dated Jurassic (836 m deep)

For the experiment carried out with samples from site Pb_J_11, the prokaryotic concentration changed slightly throughout incubation from the beginning to the end, as shown by the results obtained by quantitative PCR with a concentration of between $5.95{\cdot}10^5 \pm 4.51{\cdot}10^4$ and $1.50{\cdot}10^6 \pm 1.31{\cdot}10^6$ copy numbers of *16S rRNA* gene. mL^{-1} (Table S1). As shown in Fig. 1c and d), the microbial community was mostly composed, on day 43 of incubation, of fermenters (*Spirochaetaceae* [*Sphaerochaeta* sp.], 11%; *Dysgonomonadaceae*, 10%; *Tanneraellaceae*, 3%) and sulfate reducers (*Desulfurispora* sp., 41%; *Desulfovibrionaceae*, 16%). Furthermore, the presence of bacteria affiliated with the genus *candidatus Dichloromethanomonas* (10% on day 7) and related to the *Peptococcaceae* family (e.g., KU341776) was noteworthy. After the injection of 9% H_2 and until the end of the experiment, the fermenters belonged to the families *Spirochaetaceae* (42%), *Thermoanaerobacteraceae* (4%), and *Dysgonomonadaceae* (8%) and the genus *Pelotomaculum* (<1%). The sulfate reducers were affiliated with the genus *Desulfurispora* (3%) and the families *Ammonificaceae* (2%) and *Desulfovibrionaceae* (6%). Among these sulfate reducers, members of *Ammonificaceae* had an increase in activity following H_2 injection (7%), as did *Desulfovibrionaceae* (30%). Sequences assigned to the family *Ammonificaceae* were similar to environmental sequences found in deep subsurface environments (GU188991, JQ291343, CP034260) and related to *Desulforudis audaxviator* BYF (CP034260 [71]) and the strain KNH (AB518055 [72]). Finally, H_2 injection enabled the development of the actinobacterial lineage OPB41 (6%). Environmental sequences of this lineage are frequently found in methanogenic or hydrogen-related communities (KU998268, EU522663, FR675974) [73–75]. Although taxonomic diversity analysis, based on the *16S rRNA* gene, did not reveal the presence of methanogenic archaea, a quantitative PCR approach on DNA revealed them from day 43–78 with concentrations between $1.76 \times 10^2 \pm 4.42 \times 10^1$ to $3.32 \times 10^2 \pm 1.92 \times 10^1$ of *mcrA* gene copies. mL^{-1} (Table S1). Based on the quantification of the *mcrA* gene transcripts, their undetectable activity at the beginning of the experiment increased until day 49 ($2.27 \times 10^3 \pm 1.80 \times 10^2$ *mcrA* gene transcripts. mL^{-1}) before decreasing and becoming undetectable again at the end of the experiment. The quantification of the *dsrB* gene suggested an increase in sulfate reducers during the first 49 days of incubation (from $1.01 \times 10^5 \pm 5.96 \times 10^3$ to $6.00 \times 10^6 \pm 3.00 \times 10^5$ *dsrB* gene copies. mL^{-1}) without H_2, then a slight decrease until reaching 2.73×10^6

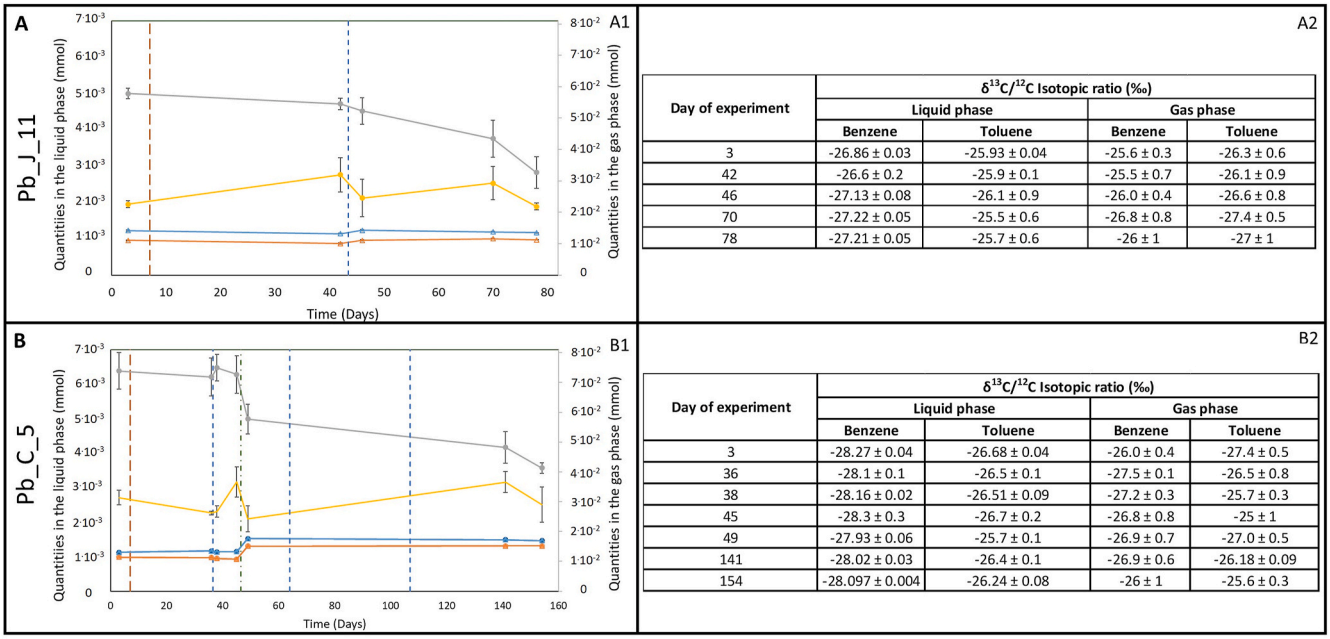

Day of experiment	$\delta^{13}C/^{12}C$ Isotopic ratio (‰)			
	Liquid phase		Gas phase	
	Benzene	Toluene	Benzene	Toluene
3	-26.86 ± 0.03	-25.93 ± 0.04	-25.6 ± 0.3	-26.3 ± 0.6
42	-26.6 ± 0.2	-25.9 ± 0.1	-25.5 ± 0.7	-26.1 ± 0.9
46	-27.13 ± 0.08	-26.1 ± 0.9	-26.0 ± 0.4	-26.6 ± 0.8
70	-27.22 ± 0.05	-25.5 ± 0.6	-26.8 ± 0.8	-27.4 ± 0.5
78	-27.21 ± 0.05	-25.7 ± 0.6	-26 ± 1	-27 ± 1

Day of experiment	$\delta^{13}C/^{12}C$ Isotopic ratio (‰)			
	Liquid phase		Gas phase	
	Benzene	Toluene	Benzene	Toluene
3	-28.27 ± 0.04	-26.68 ± 0.04	-26.0 ± 0.4	-27.4 ± 0.5
36	-28.1 ± 0.1	-26.5 ± 0.1	-27.5 ± 0.1	-26.5 ± 0.8
38	-28.16 ± 0.02	-26.51 ± 0.09	-27.2 ± 0.3	-25.7 ± 0.3
45	-28.3 ± 0.3	-26.7 ± 0.2	-26.8 ± 0.8	-25 ± 1
49	-27.93 ± 0.06	-25.7 ± 0.1	-26.9 ± 0.7	-27.0 ± 0.5
141	-28.02 ± 0.03	-26.4 ± 0.1	-26.9 ± 0.6	-26.18 ± 0.09
154	-28.097 ± 0.004	-26.24 ± 0.08	-26 ± 1	-25.6 ± 0.3

Fig. 3. Evolution of the quantities of benzene and toluene in the liquid and gas phases (first column) and the carbon isotopic ratio (second column). (A) Pb_J_11 experiment and (B) Pb_C_5 experiment. The brown, blue and green vertical lines correspond to the $CH_4 + CO_2$ reinjections, hydrogen injections and formation water reinjection, respectively. The gray and blue curves correspond to the quantity of benzene in the gas and liquid phases, respectively. The yellow and orange curves correspond to the quantity of toluene in the gas and liquid phases, respectively.

$\pm 9.32 \times 10^4$ *dsrB* gene copies. mL^{-1}. Their activity followed by the quantification of the *dsrB* gene transcripts showed the same trend.

3.4.2. *Pb_C_5, samples from a sedimentary layer dated early cretaceous (840 m deep)*

For the experiment performed with samples from the Pb_C_5 site, the prokaryotic varied little throughout the experiment, with concentrations ranging between $1.32{\cdot}10^5$ $\pm 7.57{\cdot}10^4$ and $2.05{\cdot}10^6$ $\pm 3.49{\cdot}10^5$ copy numbers of *16S rRNA* gene. mL^{-1} (Table S1). This microbial community was again mostly driven by fermenters (*Spirochaetaceae*, 41%; *Pelotomaculum*, 14%; *Caldicoprobacteriaceae*, 5%; *Dysgonomonadaceae*, 20%) and sulfate reducers (*Desulfofarcinem*, 1%; *Desulfallas*, 4%; *Desulfovibrionaceae*, 2%) (Fig. 1e and f). The presence of members of the genus *Candidatus Dichloromethanomas* was revealed before the first H_2 injection (1.90%), without substantial metabolic activity (approximately 0.1%). Three H_2 injections of approximately 2% were performed on the 36th, 64th and 107th days. Successive injections of H_2 favored mostly the families *Ammonificaceae* among the sulfate reducers (from 43% on day 50 to 15% on day 163) and *Caldicoprobacteraceae* among the fermenters (21% on day 163). At the end of the experiment, the activity of other sulfate-reducing bacteria was also demonstrated, the majority of which were affiliated with Firmicutes, as well as the *Ammonificaceae* members *Desulfotomaculum* (19%), *Desulfallas_Sporotomaculum* (2%), and *Peptococcaceae* (19%). Finally, some sulfate reducers were affiliated with the families *Desulfarculaceae* (12%) and *Desulfovibrionaceae* (2%). Quantification of *mcrA* gene copies revealed a very low concentration of methanogenic archaea, explaining their nondetection by *16S rDNA*-based approaches and an activity below the sensitivity of transcript detection by the quantitative PCR approach (Table S1). The quantity of sulfate reducers was maintained throughout the 163 days of experimentation with concentrations between $5.99.10^5$ $\pm 4.55 \times 10^4$ and 5.62×10^6 $\pm 1.45 \times 10^6$ *dsrB* gene copies. mL^{-1} and maintained their activity.

3.5. *Solid phase evolution*

3.5.1. *Pb_J_11, samples from a sedimentary layer dated Jurassic (836 m deep)*

To analyze the solid phase evolution during the Pb_J_11 experiment, the porosity of one cylinder of consolidated rock was studied. The cylinder of interest described in red in Fig. 4a, b, c and d was chosen for the analysis. The average porosity in this cylinder was 19.1 ± 1% and 20.7% ± 1% before and after the experiment, respectively. The estimation of porosity showed a slight increase after the experiment. The average porosities obtained slice by slice before and after the experiment are presented in Fig. 4e and revealed the same trend, and the gap between the initial and final porosity increased from the bottom to the top of the basket. Analyses with XRD showed that the initial rock was composed of quartz (49%), calcite (28%), microcline (8%), barite (2%), illite (10%), kaolinite (1%) and pyrite (2%) (Fig. 5). The same crystallized phases were identified at the end of the experiment, and the amount of clay minerals increased at the three depths. At the surface, middle and bottom, we identified quartz (31% for the three depths), calcite (27%, 25%, 24%), microcline (10%, 12%, 10%), barite (3% for the three depths), illite (24%, 21%, 23%), kaolinite (6%, 5%, 7%), and pyrite (3% for the three depths). The SEM/EDX approach confirmed the XRD results. Quartz, calcite, barite, and pyrite were still identified after the experiment (Fig. 6). Clays were more frequently observed than at the beginning of the experiment. No significant variation was observed in any SEM sample.

3.5.2. *Pb_C_5, samples from a sedimentary layer dated Jurassic (840 m deep)*

For the X-ray computed tomography approach, the Teflon tubing was filled with two cylinders of consolidated rock, as shown in Fig. 7e, f and g. One zone of interest was chosen for each piece of consolidated rock (cylinders A and B, as shown in Fig. 7a–g, to avoid zones with cracks on the border of the sample). The average porosities obtained in cylinders A and B were 3.3% ± 1% and 5.0% ± 1%, respectively, before the experiment and 2.7% ± 1% and 3.0% ± 1%, respectively, after the experiment. The results globally showed a slight decrease in porosity

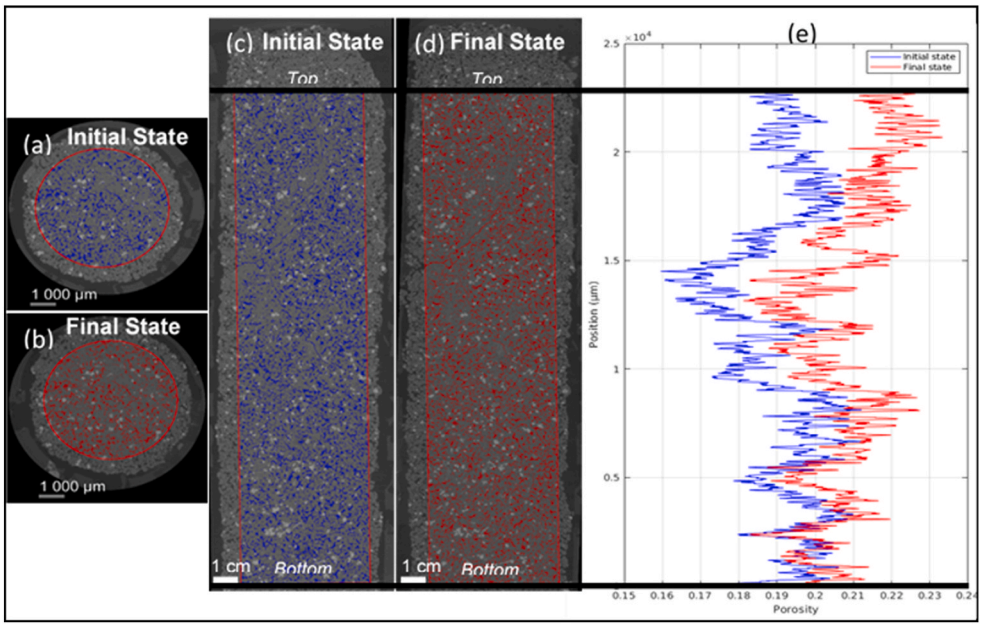

Fig. 4. (a) and (b) Examples of the same transversal X-ray computed tomography image of the consolidated rock before and after the Pb_J_11 experiment. (c) and (d) Examples of the same longitudinal X-ray computed tomography image of the consolidated rock before and after the experiment, respectively. The studied cylinder used for the analysis of porosity appears in red in (a), (b), (c) and (d), with the porosity shown in blue and red before and after the experiment, respectively. The average porosity slice by slice along the vertical axis is presented in (e).

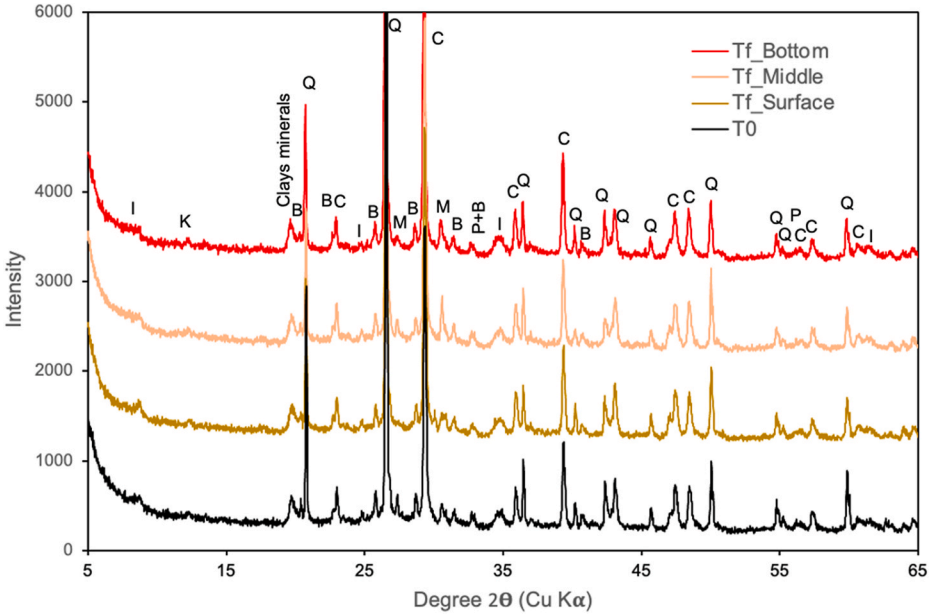

Fig. 5. X-ray diffraction patterns of samples collected at the beginning of the Pb_J_11 experiment (t_0) and at the end of the experiment (t_f) at various depths of the reactor. I: illite, K: kaolinite, Q: quartz, C: calcite, B: barite, M: microcline, P: pyrite.

after the experiment. The variation in porosity stayed in the range of uncertainties in cylinder A but reached 2% in cylinder B. These results were confirmed by the slice-by-slice analyses of the porosities before and after the experiment, which are presented in Fig. 7h and i. The global gap between the initial and final porosities stayed below 1% for cylinder A and could locally reach up to 6% in cylinder B, for example, in the bottom part and the upper part of the cylinder. XRD results revealed that the initial rock was mostly composed of quartz (72%), clay minerals including kaolinite (8%) and illite (10%), microcline (5%), albite (3%), and pyrite (2%) (Fig. 8). No significant change was observed at the end of the experiment except for a possible slight increase in illite. The proportions of quartz were 70%, 71% and 73% at the surface, middle, and bottom, respectively; microcline was 6% at the surface and 3% at the middle and bottom; albite was 3% at the three depths; and pyrite was 2% at the three depths. Kaolinite was still 7% in the surface and middle and 6% in the bottom, which was not a significant decrease. The amount of illite amounted to 12%, 15% and 13% at the surface, middle and bottom, respectively. SEM/EDX observations identified detrital quartz (1–50 µm) with local evidence of overgrowths, as well as clay phases (kaolinite, illite/smectite) as major phases (Fig. 9a–c). Other minor phases were identified: authigenic pyrites (octahedral, cuboactahedral, and often framboidal), which may be partially oxidized, and more

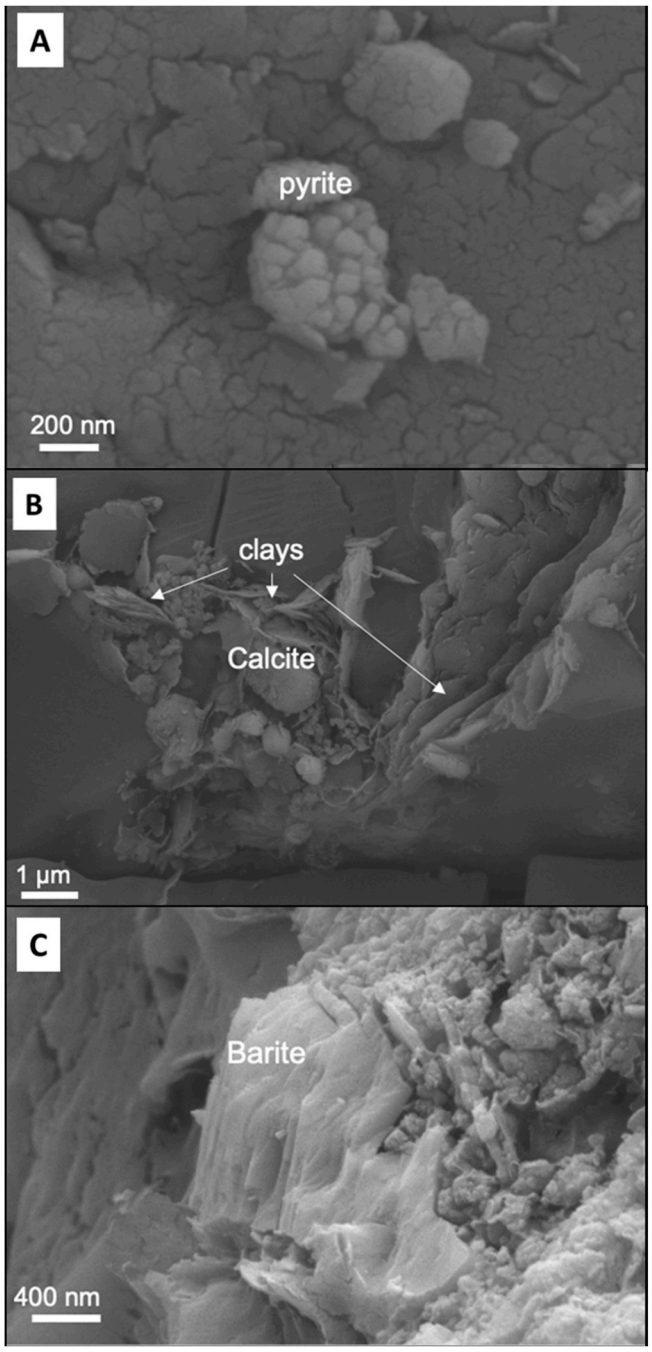

Fig. 6. SEM images of the Pb_J_11 experiment solid phase at the end of the experiment (A and B: surface depth, and C: bottom depth) showing pyrite, clay minerals and barite.

rarely, Ti oxides (globular anatase type or elongated rutile type), Fe oxides, calcite, possibly feldspars and rare monazites and zircons. Few differences were noted before and after the reaction (Fig. 9b), except that rocks seemed slightly richer in framboidal pyrite grains after the experiment (Fig. 9d). In addition, the larger pyrite grains locally showed irregular surfaces, suggesting additional growth.

3.6. Biochemical modeling

3.6.1. Reactor in situ conditions modeling

3.6.1.1. Pb_T_1, samples from a sedimentary layer dated Triassic (989 m deep). This modeling was performed with data from Haddad et al., 2022 [9]. On the first point of modeling on day 9 (Fig. 2 A3), the modeled pH (6.1) was significantly lower than that measured at atmospheric pressure (7.9) before the experiment because of the solubilization of CO_2 (1.16×10^{-2} mol. kgw^{-1}) into the formation water. The dissolved CO_2 quantities were consistent with the pH changes observed. The pH gradually increased to reach an alkaline value (8.5) at the end of experiment, which was consistent with the observed consumption of CO_2. In this experiment, H_2S was below the detection limit of 15 ppm in the gas phase; thus, only the redox potentials of the CO_2/CH_4 and H^+/H_2 couples were calculated. On day 9, the modeled redox potential of the carbon couple was −162 mV. This potential continuously decreased and bottomed at −393 mV. On day 22, after the H_2 injection, the hydrogen redox potential was −367 mV and decreased during the experiment and reached −565 mV at the end of the experiment.

3.6.1.2. Pb_J_11, samples from a sedimentary layer dated Jurassic (836 m deep). For the first experiment, the initial pH was significantly lower (6.3) (Fig. 2 B3) than the atmospheric value (8.1) at the first point because of CO_2 solubilization (1.32×10^{-2} mol. kgw^{-1}). The pH value was constant until the injection of H_2 on day 43. After H_2 injection, the pH slowly increased to 6.8 at the end of the experiment. On day 7, the carbon redox potential was −215 mV. During the experiment, the potential slightly decreased and reached −251 mV. After H_2 injection, the hydrogen potential was −419 mV and decreased until the end of the experiment (−445 mV). H_2S was first detected on day 49, and the associated redox potential was −195 mV. This potential decreased and bottomed at −223 mV at the end of the experiment.

3.6.1.3. Pb_C_5, samples from a sedimentary layer dated early Cretaceous (840 m deep). The initial pH was slightly acidic (6.2) (Fig. 2C3) because of CO_2 dissolution (1.32×10^{-2} mol. kgw^{-1}). No significant variation was observed until the first H_2 injection on day 36. After H_2 injection, the pH constantly increased to reach a maximum of 7.8 on day 154. In this experiment, the carbon redox potential was initially −198 mV and decreased to −306 mV at the end of the experiment. From the H_2 injection to the end of the experiment, the hydrogen redox potential decreased from −390 mV to −472 mV. H_2S was detected on day 43 shortly after the H_2 injection. From this day to the end of the experiment, the modeled sulfur potential decreased from −180 to −275 mV.

3.6.2. Extent of reaction equations based on microbial diversity

The stoichiometry of H_2S in Eq. (2) (liquid and gaseous) noted ν is 0.85, 0.67, and 0.56 for experiment Pb_T_1, Pb_J_11, and Pb_C_5, respectively. This result is based on the equilibrium modeling performed previously. For the Pb_T_1 experiment, sulfate reduction was considered from days 28–64, methanogenesis was considered from days 56–87, and acetogenesis and formate production were selected from injection day 28 to the end of the experiment (day 87). For the Pb_J_11 experiment, all four reactions were considered from day 49 to the end of the experiment (day 78). The Pb_C_5 experiment was the only one where methanogen activity was not detected. Sulfate reduction, acetogenesis, and formate production were considered from day 43 to the end of the experiment (day 148).

3.6.2.1. Pb_T_1, samples from a sedimentary layer dated Triassic (989 m deep). The evolution of the quantity of H_2 (Fig. 10, A1) calculated based on the microbial reactions was consistent with the experimental data. From days 29–52, no methanogenesis was considered based on the low methanogenic activity. In this period, the CO_2 quantity was an output

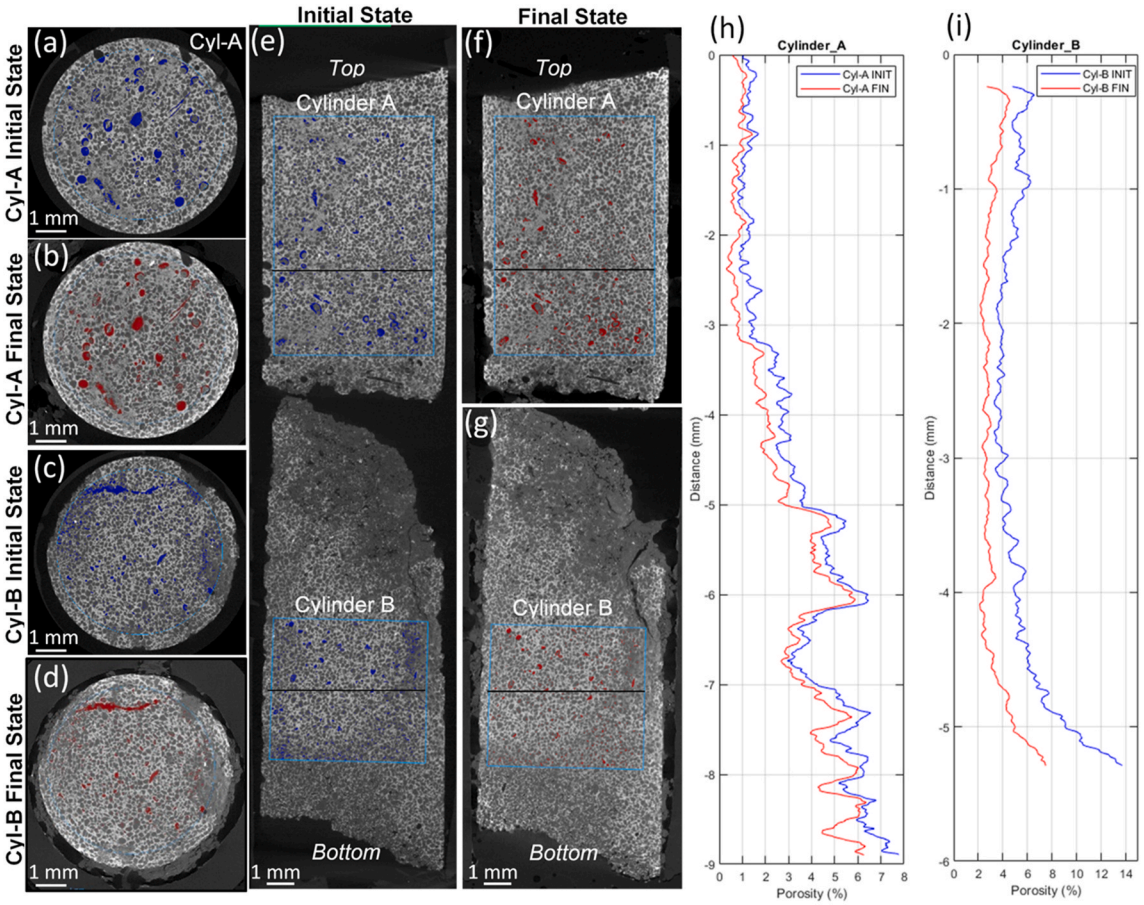

Fig. 7. Examples of the same transversal X-ray computed tomography images of the consolidated rock before and after the Pb_C_5 experiment in cylinder A (a) and (b) and cylinder B (c) and (d). Examples of the same longitudinal X-ray computed tomography image of the consolidated rock before (e) and after (f and g) the experiment. The studied cylinders A and B used for the analysis of porosity appear in (a), (b), (c), (d), (e), (f) and (g), and the corresponding porosities are shown in blue and red before and after the experiment, respectively. The average porosities obtained slice by slice along the vertical axis before and after the experiment are presented in (h) for cylinder A and in (i) for cylinder B.

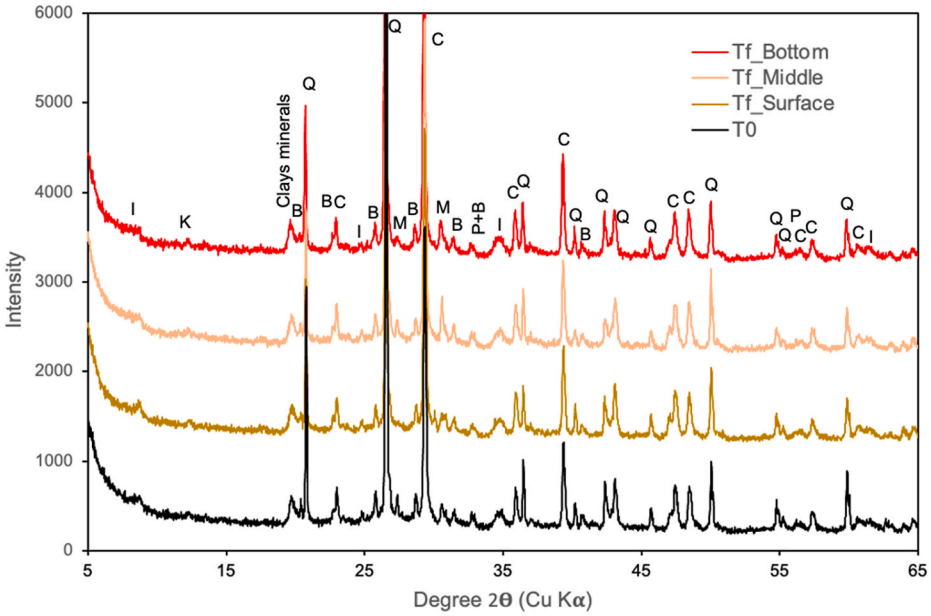

Fig. 8. X-ray diffraction patterns of samples collected at the beginning of the Pb_J_11 experiment (T_0) and at the end of the experiment (T_f) at various depths of the reactor. I: illite, K: kaolinite, Q: quartz, C: calcite, B: barite, M: microcline, P: pyrite.

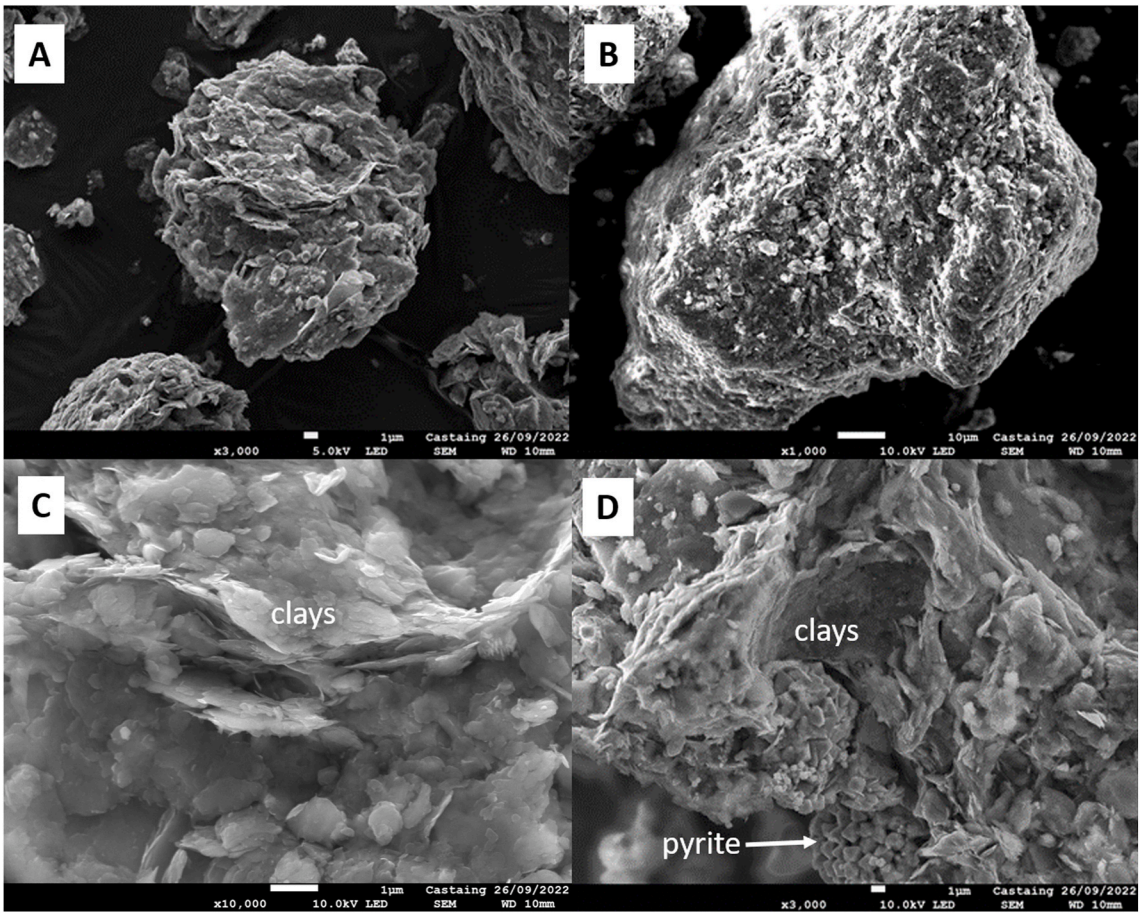

Fig. 9. SEM images of the Pb_C_5 experimental solid phase. A: Example of a grain covered by an agglomerate largely made up of clays before the experiment. B: Example of a grain covered by an agglomerate largely made up of clays after the experiment. C: Close-up view of the clays in the grain shown in A (before the experiment). D: Close-up view of the clays in the grain shown in B (after the experiment).

variable of the equation system in Eq. (B.1). The evolution of the computed CO_2 quantity in this period (Fig. 10, A2) was consistent with the experimental data. From days 29–52, H_2 consumption was mainly driven by formate production. From day 55–84, the system was mainly driven by methanogenesis, which consumed the majority of H_2.

3.6.2.2. Pb_J_11, samples from a sedimentary layer dated Jurassic (836 m deep). The evolution of the quantity of H_2 (Fig. 10, B1) calculated based on the microbial reactions was consistent with the experimental data. In this experiment, methanogen activity was observed during the entire study period. Thus, the evolution of CO_2 (Fig. 10, B2) could not be used for validation, as CO_2 was an entry variable in this case Eq. (B.1). After H_2 injection, the system was mostly driven by sulfate reduction and methanogenesis. Acetate and formate production occurred at a lower scale from H_2 injection to the end of the experiment. The calculated H_2S quantities showed a constant increase throughout the experiment, whereas the experimental value stagnated at a significantly lower value.

3.6.2.3. Pb_C_5, samples from a sedimentary layer dated early Cretaceous (840 m deep). In this experiment, the evolution of the H_2 quantity (Fig. 10, C1) that was calculated based on the microbial reactions poorly described the experimental evolution of H_2 from days 56–92. With methanogens absent, the CO_2 quantity was an output variable of the equation system. The consumption of CO_2 was slightly underestimated from days 56–92 but was still coherent with the experimental data. From day 92 to the end of the experiment, both CO_2 and H_2 modeled quantities were coherent with the experimental data. According to this model, H_2 consumption was dominated by sulfate reduction. For the Pb_J_11 experiment, the calculated H_2S quantity was did not significant from the experimental observations.

4. Discussion

In the context of H_2 sector development and its future potential storage in the UHS, Haddad and her collaborators carried out an initial study on the effect of 10% H_2 in a deep aquifer (Pb_T_1 site) [9]. They showed that H_2 injection led to formate production and that sulfate reducers dominated the microbial community in the first phase, followed by methanogenesis after sulfate was totally consumed. We assume that methanogenesis from archaea, such as *Methanobacterium* spp., consumed most of the CO_2 in this experiment (42 mmol out of 48 mmol of CO_2 consumption). Although H_2S was not detected in the gas phase, framboidal pyrite was observed by SEM after the experiment, highlighting the production of sulfide during incubation. A slight modification in porosity was observed and was attributed to clay deposition, pyrite precipitation, and calcite/barite dissolution. These results were consistent with those published in 1990 in the context of town gas storage (54% H_2, 21% CH_4, 12% CO_2, 9% CO) in a deep aquifer [7] and demonstrated significant methanogenesis from H_2 (and CO_2 and CO).

In the current study, a modeling approach was conducted using data from the previous experiment by Haddad and collaborators (2022) [9] from the Pb_T_1 site. At the beginning of the experiment, the liquid–gas equilibrium modeling showed that CO_2 dissolution led to an acidic pH (6.1). This acidity could explain the development of most microorganisms, as their optimal pH for growth typically ranges from 6.1 to 7.6 [63]. The extent of the reaction equations further supported the

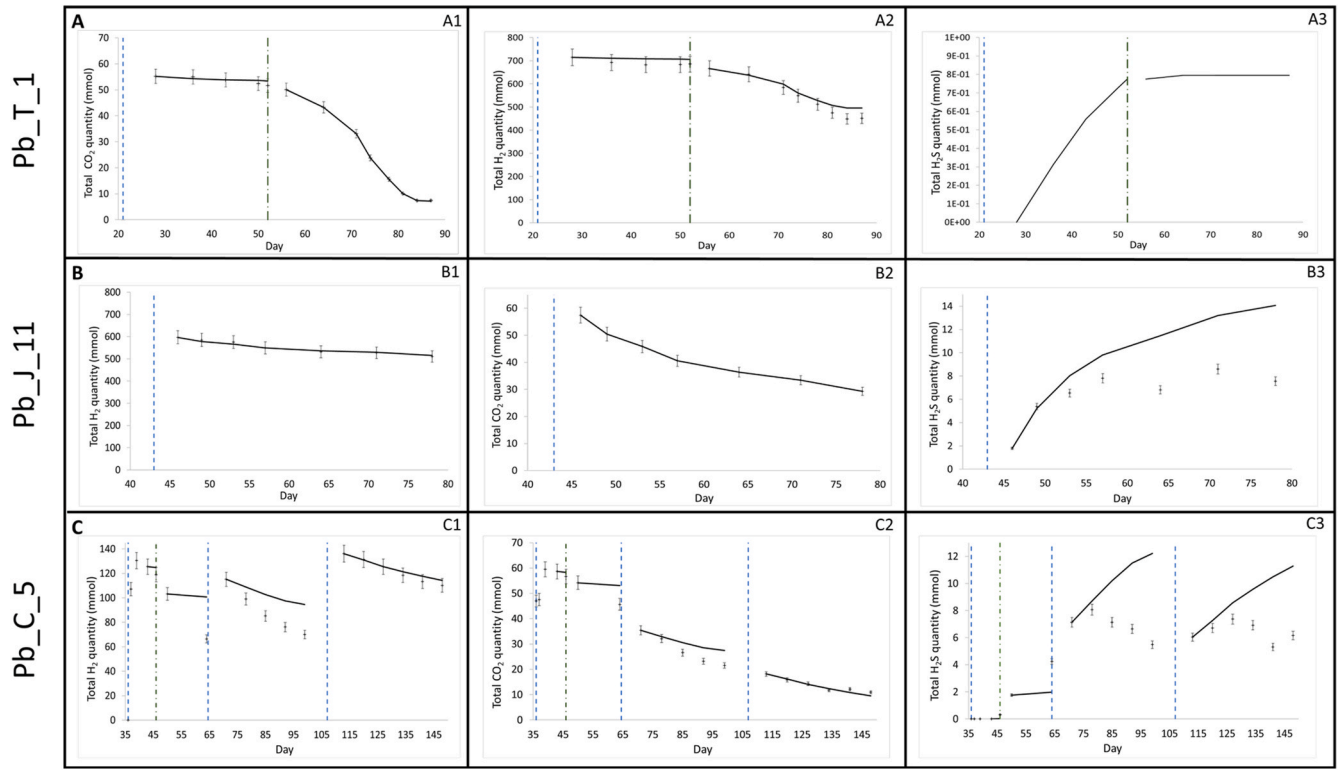

Fig. 10. Comparison of the evolution of experimental and modeled H_2, CO_2, and H_2S quantities during the experiments. Columns 1, 2, and 3 represent the evolution of total quantity (liquid and gas phase) of H_2, CO_2, and H_2S during the experiment, respectively. Lines 1, 2 and 3 represent the (A) Pb_T_1, (B) Pb_J_11, and (C) Pb_C_5 experiments, respectively. The blue and green vertical lines correspond to hydrogen injections and formation water reinjections, respectively. The experimental data are represented by the cross. The black curve represents the quantities of matter modeled by the extent of reaction equations. No experimental data are shown in Fig. A3 as H_2S was not detected in this experiment.

occurrence of sulfate reduction, methanogenesis, formate production, and acetogenesis by showing good agreement between the modeled H_2 consumption and the experimental values.

Few studies have investigated the effect of H_2 on UGSs, such as deep aquifers [7,9,32,34,76], even though these aquifers may represent most storage structures in several countries, such as France [77]. Here, two new UGSs in deep aquifers were explored in the context of H_2 injection at a molar percentage of 9% in the case of the Pb_J_11 site and three times 2% H_2 in the case of the Pb_C_5 site. In both cases, salt concentrations, particularly sulfate, were higher than at Pb_T_1 (Pb_T_1: 0.15 mmol L^{-1} < Pb_J_11: 13.03 mmol L^{-1} < Pb_C_5: 25.06 mmol L^{-1}). Some CO_2 has served as a carbon source and even as an electron acceptor for hydrogenotrophic microorganisms. Moreover, a disappearance of CO_2 was also associated with an alkalinisation of the liquid phase, an expected phenomenon in the presence of methanogenesis and amplified here by (homo)-acetogenesis and sulfate-reduction based on hydrogenotrophy. The increase in *in situ* pH could be limiting for microbial growth, as the maximum pH for optimal growth of sulfate reducers was shown to be 7.4 [63]. This is particularly relevant in the Pb_C_5 experiment, in which the modeled pH reached 7.8 at the end of the experiment, potentially leading to a decrease in microbial activities. Solving the reaction equations showed that the stoichiometry of the previously cited reactions explained the evolution of CO_2 in all experiments, further supporting the microbial origin of this consumption. For all experiments, despite H_2 consumption, the redox potential of all couples continuously decreased. This could be explained by the evolution of pH spanning multiple orders of magnitude, whereas species generally stay in the same position. In the example of the sulfur potential, a variation of 4 orders of magnitude in the HS^-/SO_4^{2-} ratio would lead to only a 20 mV variation in the potential [60].

Several taxonomic groups identified in these three experiments have been described as harboring acetogens, such as families of *Clostridiaceae, Eubacteriaceae* or Acidobacteria [78,79]. In each case, the injection of H_2 resulted in the appearance of formate, which we assume is linked, in part or in whole, to the effect of pressure on acetogenic bacterial metabolism. Indeed, Stoll and collaborators [11] demonstrated that an increase in pressure (1–7 bar) caused *Clostridium Ijungdahlii* activity to shift from acetate to formate production. It is hypothesized that the high partial pressure of CO_2 in the reactor results in greater diffusion of the molecule across the cellular membrane, leading to acidification of the bacterial cytoplasm. The resulting reduction in membrane potential would lead to a drop in energy production and the impossibility of carrying the metabolic pathway through to acetate (*i.e.*, formate accumulation).

Although the resources of energy/electron donors (*i.e.*, H_2), carbon (*i.e.*, CO_2 and carbonates) and electron acceptors (*i.e.*, SO_4^{2-}, CO_2) remained in sufficient quantities during the whole Pb_J_11 and Pb_C_5 experiments, the microbial communities studied in both experiments appeared limited in their development, and the rates of the microbial reactions decreased toward the end of the experiment after 57 or 120 days of incubation. Indeed, prokaryotic concentrations estimated by qPCR approaches based on the *16S rRNA* gene remained remarkably stable throughout the experiments, suggesting a growth limitation by other nutrients, such as ammonium, phosphate or metals, that we did not track. If this hypothesis is verified under *in situ* conditions, it will be imperative to consider this criterion in future simulations of the evolution of H_2 storage in aquifers. Although studies have shown that formate inhibits sulfate-reduction growth at concentrations above 8 mM [80], lower concentrations in the current experiments do not suggest such an action (Pb_J_11: 2.55 mM; Pb_C_5: 0.37 mM).

While sulfate was totally consumed (and barite dissolved) in a previous experiment [9], *i.e.*, $2.51 \pm 1.25 \times 10^{-1}$ mmol sulfate, this was not the case for the two experiments in this study. The quantity of H_2S was

lower than the modeled values for each experiment. In the Pb_J_11 and Pb_C_5 experiments, 14.1 and 10.3 mmol of H_2S should have been produced by sulfate reduction, whereas the maximal quantities observed experimentally were 8.6 and 8.1 mmol. Notably, the experimental value includes modeled dissolved sulfide, whose quantity is influenced by the evaluation of *in situ* pH. This phenomenon could be triggered by the precipitation of iron sulfide, lowering the free quantity of H_2S in the reactor. This hypothesis is supported by the observation of an increased quantity of framboidal pyrite with SEM in the Pb_T_1 and Pb_J_11 experiments, which is characteristic of microbially induced pyrite. Numerous precipitates, identified by XRD as pyrite, were also found on the internal surfaces of the HP reactor, the basket and the agitation system (data not shown).

As far as the results of modeling are concerned, a good fit was obtained for experiments Pb_T_1 and Pb_J_11 regarding H_2 consumption. The set of microbial reactions chosen to model the evolution of the quantities of matter largely underestimated H_2 consumption for the first part of the Pb_C_5 experiment. An increase in magnesium ions was noted during this period. Abiotic tests showed that Mg^{2+} and SO_4^{2-} could be released simultaneously by the rock (data not shown). Epsomite ($MgSO_4$) was not detected by XRD, which could be because Mg^{2+} and SO_4^{2-} were released by a combination of dissolution and precipitation reactions. If this mineral did dissolve, sulfate reduction would have happened in larger quantities, explaining the H_2 loss observed. This hypothesis is supported by the coherence of CO_2 consumption and HCO_3^- production with H_2 loss. Sulfide production was also observed in this period (2.3 mmol).

In the Pb_J_11 and Pb_C_5 experiments, benzene and toluene did not appear to have been consumed by microorganisms (Fig. 3), although their degradation has been demonstrated previously at these sites [81]. Two hypotheses may be put forward to explain this result: i) an incubation time (*i.e.*, 80 and 160 days) that is too short compared with the experiments carried out over more than 800 days, which demonstrated the potential for degradation; and ii) an inhibitory effect of H_2 that remains to be determined but could favor microorganisms incapable of biodegrading these monoaromatic hydrocarbons.

The slight increase in porosity observed by X-ray computed tomography during the Pb_J_11 experiment is unlikely to originate from mineral dissolution. Contrary to the results of the Pb_T_1 experiment, calcite and barite did not seem to have been partially dissolved. This result is consistent with physico-chemical analyses, as no calcium ion increase was noted. One hypothesis of the origin of this porosity change could be the transport of fine particles by the liquid phase. In the Pb_C_5 experiment, the slight increase in illite observed by XRD could be related to the low decrease in porosity observed by X-ray computed tomography.

The reactor can be compared to the microbial ecosystem of the aquifer's microporous rock, with a very slow water circulation on the order of 1 m per year [82,83]. In each experiment, the consumption of H_2 over the course of 34–112 days was important (41%, 15% and 49%). However, the rate of consumption could be lower in aquifers, as the methanogenesis rate in the Lobodice storage was 4–50 times slower than laboratory rates [32]. The production of H_2S observed in Pb_J_11 and Pb_C_5 could lead to corrosion of infrastructures and decrease the quality of withdrawn H_2 and natural gas. In this sense, the Pb_T_1 site seems more suited to safely store H_2, as no H_2S was detected. Globally, to avoid souring and corrosion induced by sulfate reduction, low sulfate sites are indicated. However, methanogenesis in Pb_T_1 did consume H_2 at a higher rate than that observed with sulfate reduction. Pyrite and clay precipitation are to be expected in each site, but the induced porosity changes were shown to remain small, inducing little impact on the reservoir.

5. Summary and conclusions

The feasibility and safety of H_2 storage in deep aquifers depend on several factors.

- Microbial hydrogenotrophic activity could be inhibited or limited, potentially by a lack of nutrient elements or electron acceptors.
- In sulfate-rich sites, H_2S is to be expected and could potentially reach high concentrations, causing corrosion issues on infrastructures and requiring gas treatment at withdrawal.
- Buffering of H_2S could occur, possibly through pyrite precipitation.
- Dissolution and precipitation of minerals are expected but do not show a drastic change in porosity for the studied sites.
- To limit the undesirable impacts of H_2 injection in deep aquifers, storage containing low amounts of sulfate and sulfate-bearing minerals should be preferred, as H_2S production will be lower.
- UGS with a high proportion of carbonated minerals may support greater autotrophic microbial activity.

Although not clearly identified, inhibiting factors appear to limit microbial activity. Thus, microbial activity should be slower by low ammonium or phosphate ions, or the pH increase induced by microbial activities.

Author contributions statement

MRP, FC, PCe and ARP co-conceived the study. JM, PGH, MD, FC, PCe carried out the high pressure and simulation experiments. MRP, MG, AB, AL and ARP applied the microbiological approaches. PS, M − PI, PM and GH used the imaging and mineralogical characterization. ML and ILH analyzed the hydrocarbons. All authors contributed in the interpretation of results and paper writing.

Declaration of competing interest

The authors declare that they have no known competing financial interests or personal relationships that could have appeared to influence the work reported in this paper.

Acknowledgments

Enagas, SNAM, Storengy and Teréga are acknowledged for funding this research project. We are grateful to the Genotoul platform (genotoul.fr) for the sequencing analyses. MRP salary was supported by E2S-UPPA. AL salary was supported by Agence Nationale de la Recherche (ANR-20-CHIN-0001-01) and Engie in the ORHYON industrial chair. We thank the Bordeaux Imaging Center, and particularly Isabelle Svahn, for her help in the SEM-EDX analysis. We would also like to thank TotalEnergies for providing UMS 3360 DMEX with the Zeiss Xradia Versa 510 which carried out the tomographic acquisitions reported in this article.

Nomenclature

H_2	Hydrogen
UGS	Underground gas storage
UHS	Underground hydrogen storage
CO_2	Carbon dioxide
CH_4	Methane
HP	High pressure
H_2S	Hydrogen sulfide
CSIA	Compounds Specific Isotope Analysis
BT	Benzene and Toluene
PCR	Polymerase Chain Reaction
PES	Polyethersulphone
rRNA	Ribosomal ribonucleic acid
DNA	Deoxyribonucleic acid
cDNA	Complementary deoxyribonucleic acid
NCBI SRA	National Institutes of Health sequence read archive
XRD	X-ray diffraction

SEM/EDX Scanning electron microscopy with energy-dispersive X-ray spectroscopy

Appendix A. Supplementary data

Supplementary data to this article can be found online at https://doi.org/10.1016/j.ijhydene.2024.02.322.

Appendix A. Thermodynamic modeling

.

Appendix B. Extent of reaction equations

.

References

[1] Iordache I, Schitea D, Gheorghe AV, Iordache M. Hydrogen underground storage in Romania, potential directions of development, stakeholders and general aspects. Int J Hydrogen Energy 2014;39:11071–81. https://doi.org/10.1016/j.ijhydene.2014.05.067.

[2] Edelenbosch OY, McCollum DL, van Vuuren DP, Bertram C, Carrara S, Daly H, et al. Decomposing passenger transport futures: comparing results of global integrated assessment models. Transp Res Part Transp Environ 2017;55:281–93. https://doi.org/10.1016/j.trd.2016.07.003.

[3] Hanley ES, Deane J, Gallachóir BÓ. The role of hydrogen in low carbon energy futures–A review of existing perspectives. Renew Sustain Energy Rev 2018;82:3027–45. https://doi.org/10.1016/j.rser.2017.10.034.

[4] Lazarou S, Vita V, Diamantaki M, Karanikolou-Karra D, Fragoyiannis G, Makridis S, et al. A simulated roadmap of hydrogen technology contribution to climate change mitigation based on Representative Concentration Pathways considerations. Energy Sci Eng 2018;6:116–25. https://doi.org/10.1002/ese3.194.

[5] McPherson M, Johnson N, Strubegger M. The role of electricity storage and hydrogen technologies in enabling global low-carbon energy transitions. Appl Energy 2018;216:649–61. https://doi.org/10.1016/j.apenergy.2018.02.110.

[6] Pastore LM, Lo Basso G, Quarta MN, de Santoli L. Power-to-gas as an option for improving energy self-consumption in renewable energy communities. Int J Hydrogen Energy 2022;47:29604–21. https://doi.org/10.1016/j.ijhydene.2022.06.287.

[7] Šmigáň P, Greksák M, Kozánková J, Buzek F, Onderka V, Wolf I. Methanogenic bacteria as a key factor involved in changes of town gas stored in an underground reservoir. FEMS Microbiol Lett 1990;73:221–4. https://doi.org/10.1016/0378-1097(90)90733-7.

[8] Dopffel N, Jansen S, Gerritse J. Microbial side effects of underground hydrogen storage – knowledge gaps, risks and opportunities for successful implementation. Int J Hydrogen Energy 2021;46:8594–606. https://doi.org/10.1016/j.ijhydene.2020.12.058.

[9] Haddad PG, Ranchou-Peyruse M, Guignard M, Mura J, Casteran F, Ronjon-Magand L, et al. Geological storage of hydrogen in deep aquifers – an experimental multidisciplinary study. Energy Environ Sci 2022;15:3400–15. https://doi.org/10.1039/D2EE00765G.

[10] Ebrahimiyekta A. Characterization of geochemical interactions and migration of hydrogen in sandstone sedimentary formations: application to geological storage. PhD Thesis. 2017.

[11] Stoll IK, Herbig S, Zwick M, Boukis N, Sauer J, Neumann A, et al. Fermentation of h2 and co2 with clostridium ljungdahlii at elevated process pressure first experimental results. Chem Eng Trans 2018;64:151–6. https://doi.org/10.3303/CET1864026.

[12] Navaid HB, Emadi H, Watson M. A comprehensive literature review on the challenges associated with underground hydrogen storage. Int J Hydrogen Energy 2023;48:10603–35. https://doi.org/10.1016/j.ijhydene.2022.11.225.

[13] Ulrich GA, Breit GN, Cozzarelli IM, Suflita JM. Sources of sulfate supporting anaerobic metabolism in a contaminated aquifer. Environ Sci Technol 2003;37:1093–9. https://doi.org/10.1021/es011288a.

[14] Dupraz S, Parmentier M, Ménez B, Guyot F. Experimental and numerical modeling of bacterially induced pH increase and calcite precipitation in saline aquifers. Chem Geol 2009;265:44–53. https://doi.org/10.1016/j.chemgeo.2009.05.003.

[15] Liu N, Kovscek AR, Fernø MA, Dopffel N. Pore-scale study of microbial hydrogen consumption and wettability alteration during underground hydrogen storage. Front Energy Res 2023;11:1124621. https://doi.org/10.3389/fenrg.2023.1124621.

[16] Jangda Z, Menke H, Busch A, Geiger S, Bultreys T, Lewis H, et al. Pore-scale visualization of hydrogen storage in a sandstone at subsurface pressure and temperature conditions: trapping, dissolution and wettability. J Colloid Interface Sci 2023;629:316–25. https://doi.org/10.1016/j.jcis.2022.09.082.

[17] Mirchi V, Dejam M, Alvarado V. Interfacial tension and contact angle measurements for hydrogen-methane mixtures/brine/oil-wet rocks at reservoir conditions. Int J Hydrogen Energy 2022;47:34963–75. https://doi.org/10.1016/j.ijhydene.2022.08.056.

[18] Zeng L, Hosseini M, Keshavarz A, Iglauer S, Lu Y, Xie Q. Hydrogen wettability in carbonate reservoirs: implication for underground hydrogen storage from geochemical perspective. Int J Hydrogen Energy 2022;47:25357–66. https://doi.org/10.1016/j.ijhydene.2022.05.289.

[19] Gbadamosi AO, Muhammed NS, Patil S, Al Shehri D, Haq B, Epelle EI, et al. Underground hydrogen storage: a critical assessment of fluid-fluid and fluid-rock interactions. J Energy Storage 2023;72:108473.

[20] Pan B, Yin X, Iglauer S. Rock-fluid interfacial tension at subsurface conditions: implications for H2, CO2 and natural gas geo-storage. Int J Hydrogen Energy 2021;46:25578–85.

[21] Tarkowski R, Uliasz-Misiak B. Towards underground hydrogen storage: a review of barriers. Renew Sustain Energy Rev 2022;162:112451.

[22] Thiyagarajan SR, Emadi H, Hussain A, Patange P, Watson M. A comprehensive review of the mechanisms and efficiency of underground hydrogen storage. J Energy Storage 2022;51:104490.

[23] Dohrmann Anja B, Krüger M. Microbial H2 consumption by a formation fluid from a natural gas field at high-pressure conditions relevant for underground H2 storage. Environ Sci Technol 2023;57:1092–102. https://doi.org/10.1021/acs.est.2c07303.

[24] Miocic J, Heinemann N, Edlmann K, Scafidi J, Molaei F, Alcalde J. Underground hydrogen storage: a review. SP528-2022–88 Geol Soc Lond Spec Publ 2023;528. https://doi.org/10.1144/SP528-2022-88.

[25] Reitenbach V, Ganzer L, Albrecht D, Hagemann B. Influence of added hydrogen on underground gas storage: a review of key issues. Environ Earth Sci 2015;73:6927–37. https://doi.org/10.1007/s12665-015-4176-2.

[26] Stolten D, Emonts B. Hydrogen science and engineering, 2 volume set: materials, processes, systems, and technology. John Wiley & Sons; 2016.

[27] Muhammed NS, Haq B, Al Shehri D, Al-Ahmed A, Rahman MM, Zaman E. A review on underground hydrogen storage: insight into geological sites, influencing factors and future outlook. Energy Rep 2022;8:461–99. https://doi.org/10.1016/j.egyr.2021.12.002.

[28] Hematpur H, Abdollahi R, Rostami S, Haghighi M, Blunt MJ. Review of underground hydrogen storage: concepts and challenges. Adv Geo-Energy Res 2023;7:111–31. https://doi.org/10.46690/ager.2023.02.05.

[29] Pichler M. Underground sun storage results and outlook. EAGEDGMK jt. Workshop Undergr. Storage Hydrog. Celle, Germany: European Association of Geoscientists & Engineers; 2019. p. 1–4. https://doi.org/10.3997/2214-4609.201900257.

[30] HyUSPRe n.d. https://www.hyuspre.eu/ (accessed May 2, 2023).

[31] Hystories - Hydrogen Storage in European Subsurface - Hystories n.d. https://hystories.eu/ (accessed May 11, 2023).

[32] Tremosa J, Jakobsen R, Le Gallo Y. Assessing and modeling hydrogen reactivity in underground hydrogen storage: a review and models simulating the Lobodice town gas storage. Front Energy Res 2023:11. https://doi.org/10.3389/fenrg.2023.1145978.

[33] Strobel G, Hagemann B, Lüddeke CT, Ganzer L. Coupled model for microbial growth and phase mass transfer in pressurized batch reactors in the context of underground hydrogen storage. Front Microbiol 2023;14:1150102. https://doi.org/10.3389/fmicb.2023.1150102.

[34] Hassannayebi N, Azizmohammadi S, De Lucia M, Ott H. Underground hydrogen storage: application of geochemical modelling in a case study in the Molasse Basin, Upper Austria. Environ Earth Sci 2019;78:177. https://doi.org/10.1007/s12665-019-8184-5.

[35] Jahanbani Veshareh M, Thaysen EM, Nick HM. Feasibility of hydrogen storage in depleted hydrocarbon chalk reservoirs: assessment of biochemical and chemical effects. Appl Energy 2022;323:119575. https://doi.org/10.1016/j.apenergy.2022.119575.

[36] Mirchi V, Dejam M, Alvarado V, Akbarabadi M. Effect of cushion gas on hydrogen/brine flow behavior in oil-wet rocks with application to hydrogen storage in depleted oil and gas reservoirs. Energy Fuels 2023;37:15231–43.

[37] Buzek F, Onderka V, Vancura P, Wolf I. Carbon isotope study of methane production in a town gas storage reservoir. Fuel 1994;73:747–52. https://doi.org/10.1016/0016-2361(94)90019-1.

[38] Pankhurst ES. The growth and occurrence of sulphate-reducing bacteria, with particular reference to their importance in the gas industry. 1967.

[39] Foh S, Novil M, Rockar E, Randolph P. Underground hydrogen storage. Final report. [Salt caverns, excavated caverns, aquifers and depleted fields]. 1979. https://doi.org/10.2172/6536941.

[40] Ranchou-Peyruse M, Auguet J, Mazière C, Restrepo-Ortiz CX, Guignard M, Dequidt D, et al. Geological gas-storage shapes deep life. Environ Microbiol 2019;21:3953–64. https://doi.org/10.1111/1462-2920.14745.

[41] Pérez A, Pérez E, Dupraz S, Bolcich J. Patagonia wind-hydrogen project: underground storage and methanation. In: 21st world hydrog. Energy conf; 2016.

[42] Strobel G, Hagemann B, Huppertz TM, Ganzer L. Underground bio-methanation: concept and potential. Renew Sustain Energy Rev 2020;123:109747. https://doi.org/10.1016/j.rser.2020.109747.

[43] Liebscher A, Wackerl J, Streibel M. Geologic storage of hydrogen – fundamentals, processing, and projects. In: ProfDrD Stolten, Emonts DrB, editors. Hydrog. sci. eng. mater. process. syst. technol. first ed. Wiley; 2016. p. 629–58. https://doi.org/10.1002/9783527674268.ch26.

[44] Vasile NS, Bellini R, Bassani I, Vizzarro A, Abdel Azim A, Coti C, et al. Innovative high pressure/high temperature, multi-sensing bioreactors system for microbial risk assessment in underground hydrogen storage. Int J Hydrogen Energy 2024;51:41–50. https://doi.org/10.1016/j.ijhydene.2023.10.245.

[45] Saeed M, Jadhawar P, Bagala S. Geochemical effects on storage gases and reservoir rock during underground hydrogen storage: a depleted North Sea oil reservoir case study. Hydrogen 2023;4:323–37. https://doi.org/10.3390/hydrogen4020023.

[46] Amid A, Mignard D, Wilkinson M. Seasonal storage of hydrogen in a depleted natural gas reservoir. Int J Hydrogen Energy 2016;41:5549–58. https://doi.org/10.1016/j.ijhydene.2016.02.036.
[47] Hagemann B, Rasoulzadeh M, Panfilov M, Ganzer L, Reitenbach V. Hydrogenization of underground storage of natural gas: impact of hydrogen on the hydrodynamic and bio-chemical behavior. Comput Geosci 2016;20:595–606. https://doi.org/10.1007/s10596-015-9515-6.
[48] Hogeweg S, Strobel G, Hagemann B. Benchmark study for the simulation of underground hydrogen storage operations. Comput Geosci 2022;26:1367–78. https://doi.org/10.1007/s10596-022-10163-5.
[49] Haddad PG, Mura J, Castéran F, Guignard M, Ranchou-Peyruse M, Sénéchal P, et al. Biological, geological and chemical effects of oxygen injection in underground gas storage aquifers in the setting of biomethane deployment. Sci Total Environ 2022;806:150690. https://doi.org/10.1016/j.scitotenv.2021.150690.
[50] Ranchou-Peyruse M, Guignard M, Haddad PG, Robin S, Boesch F, Lanot M, et al. A deep continental aquifer downhole sampler for microbiological studies. Front Microbiol 2023;13:1012400. https://doi.org/10.3389/fmicb.2022.1012400.
[51] Fischer A, Manefield M, Bombach P. Application of stable isotope tools for evaluating natural and stimulated biodegradation of organic pollutants in field studies. Curr Opin Biotechnol 2016;41:99–107.
[52] Ponsin V, Buscheck TE, Hunkeler D. Heart-cutting two-dimensional gas chromatography–isotope ratio mass spectrometry analysis of monoaromatic hydrocarbons in complex groundwater and gas-phase samples. J Chromatogr A 2017;1492:117–28.
[53] Caporaso JG, Kuczynski J, Stombaugh J, Bittinger K, Bushman FD, Costello EK, et al. QIIME allows analysis of high-throughput community sequencing data. Nat Methods 2010;7:335–6. https://doi.org/10.1038/nmeth.f.303.
[54] Callahan BJ, McMurdie PJ, Rosen MJ, Han AW, Johnson AJA, Holmes SP. DADA2: high-resolution sample inference from Illumina amplicon data. Nat Methods 2016;13:581–3.
[55] Parkhurst DL. User's guide to PHREEQC : a computer program for speciation, reaction-path, advective-transport, and inverse geochemical calculations. Lakewood, Colo. : U.S. Dept. of the Interior, U.S. Geological Survey. Denver, CO: Earth Science Information Center, Open-File Reports Section [distributor], 1995;1995.
[56] Haghi RK, Chapoy A, Peirera LMC, Yang J, Tohidi B. pH of CO 2 saturated water and CO 2 saturated brines: experimental measurements and modelling. Int J Greenh Gas Control 2017;66:190–203. https://doi.org/10.1016/j.ijggc.2017.10.001.
[57] Peng D-Y, Robinson DB. A new two-constant equation of state. Ind Eng Chem Fundam 1976;15:59–64. https://doi.org/10.1021/i160057a011.
[58] Stefánsson A, Arnórsson S, Sveinbjörnsdóttir ÁE. Redox reactions and potentials in natural waters at disequilibrium. Chem Geol 2005;221:289–311. https://doi.org/10.1016/j.chemgeo.2005.06.003.
[59] Ioka S, Sakai T, Igarashi T, Ishijima Y. Long-term continuous in situ potentiometrically measured redox potential in anoxic groundwater with high methane and iron contents. Environ Earth Sci 2011;64:143–9. https://doi.org/10.1007/s12665-010-0830-x.
[60] Lindberg RD, Runnells DD. Ground water redox reactions: an analysis of equilibrium state applied to Eh measurements and geochemical modeling. Science 1984;225:925–7. https://doi.org/10.1126/science.225.4665.925.
[61] Panfilov M. Underground storage of hydrogen: in situ self-organisation and methane generation. Transport Porous Media 2010;85:841–65. https://doi.org/10.1007/s11242-010-9595-7.
[62] Hemme C, van Berk W. Hydrogeochemical modeling to identify potential risks of underground hydrogen storage in depleted gas fields. Appl Sci 2018;8:2282. https://doi.org/10.3390/app8112282.
[63] Thaysen E, McMahon S, Strobel GJ, Butler I, Heinemann N, Ngwenya B, et al. Estimating microbial growth and hydrogen consumption in hydrogen storage in porous media. Renew Sustain Energy Rev 2021;151:111481. https://doi.org/10.1016/j.rser.2021.111481.
[64] van Houten RT, Pol LWH, Lettinga G. Biological sulphate reduction using gas-lift reactors fed with hydrogen and carbon dioxide as energy and carbon source. Biotechnol Bioeng 1994;44:586–94. https://doi.org/10.1002/bit.260440505.
[65] Gregory SP, Barnett MJ, Field LP, Milodowski AE. Subsurface microbial hydrogen cycling: natural occurrence and implications for industry. Microorganisms 2019;7. https://doi.org/10.3390/microorganisms7020053.
[66] Rabii A, Aldin S, Dahman Y, Elbeshbishy E. A review on anaerobic Co-digestion with a focus on the microbial populations and the effect of multi-stage digester configuration. Energies 2019;12:1106. https://doi.org/10.3390/en12061106.
[67] Logroño W, Nikolausz M, Harms H, Kleinsteuber S. Physiological effects of 2-bromoethanesulfonate on hydrogenotrophic pure and mixed cultures. Microorganisms 2022;10:355. https://doi.org/10.3390/microorganisms10020355.
[68] Mancini SA, Ulrich AC, Lacrampe-Couloume G, Sleep B, Edwards EA, Lollar BS. Carbon and hydrogen isotopic fractionation during anaerobic biodegradation of benzene. Appl Environ Microbiol 2003;69:191–8.
[69] Darracq G, Couvert A, Couriol C, Amrane A, Le Cloirec P. Absorption and biodegradation of hydrophobic volatile organic compounds: determination of Henry's constants and biodegradation levels. Water Sci Technol 2009;59:1315–22.
[70] Braeckevelt M, Fischer A, Kästner M. Field applicability of Compound-Specific Isotope Analysis (CSIA) for characterization and quantification of in situ contaminant degradation in aquifers. Appl Microbiol Biotechnol 2012;94:1401–21.
[71] Karnachuk OV, Frank YA, Lukina AP, Kadnikov VV, Beletsky AV, Mardanov AV, et al. Domestication of previously uncultivated Candidatus Desulforudis audaxviator from a deep aquifer in Siberia sheds light on its physiology and evolution. ISME J 2019;13:1947–59.
[72] Nakamura K, Tamaki H, Kang MS, Mochimaru H, Lee S-T, Nakamura K, et al. A six-well plate method: less laborious and effective method for cultivation of obligate anaerobic microorganisms. Microb Environ 2011;26:301–6.
[73] Croese E, Pereira MA, Euverink G-JW, Stams AJ, Geelhoed JS. Analysis of the microbial community of the biocathode of a hydrogen-producing microbial electrolysis cell. Appl Microbiol Biotechnol 2011;92:1083–93.
[74] Marone A, Ayala-Campos OR, Trably E, Carmona-Martínez AA, Moscoviz R, Latrille E, et al. Coupling dark fermentation and microbial electrolysis to enhance bio-hydrogen production from agro-industrial wastewaters and by-products in a bio-refinery framework. Int J Hydrogen Energy 2017;42:1609–21.
[75] Siddique T, Penner T, Klassen J, Nesbø C, Foght JM. Microbial communities involved in methane production from hydrocarbons in oil sands tailings. Environ Sci Technol 2012;46:9802–10.
[76] Raad SM, Ranjbar E, Hassanzadeh H, Leonenko Y. Hydrogen-brine mixture PVT data for reservoir simulation of hydrogen storage in deep saline aquifers. Int J Hydrogen Energy 2023;48:696–708. https://doi.org/10.1016/j.ijhydene.2022.09.222.
[77] Zivar D, Kumar S, Foroozesh J. Underground hydrogen storage: a comprehensive review. Int J Hydrogen Energy 2021;46:23436–62. https://doi.org/10.1016/j.ijhydene.2020.08.138.
[78] Kielak AM, Barreto CC, Kowalchuk GA, Veen JA van, Kuramae EE. The ecology of Acidobacteria: moving beyond genes and genomes. Front Microbiol 2016;7. https://doi.org/10.3389/fmicb.2016.00744.
[79] Karekar S, Stefanini R, Ahring B. Homo-acetogens: their metabolism and competitive relationship with hydrogenotrophic methanogens. Microorganisms 2022;10. https://doi.org/10.3390/microorganisms10020397.
[80] Voskuhl L, Brusilova D, Brauer VS, Meckenstock RU. Inhibition of sulfate-reducing bacteria with formate. FEMS Microbiol Ecol 2022;98. https://doi.org/10.1093/femsec/fiac003. fiac003.
[81] Ranchou-Peyruse M, Gasc C, Guignard M, Aüllo T, Dequidt D, Peyret P, et al. The sequence capture by hybridization: a new approach for revealing the potential of mono-aromatic hydrocarbons bioattenuation in a deep oligotrophic aquifer. Microb Biotechnol 2017;10:469–79. https://doi.org/10.1111/1751-7915.12426.
[82] Jost A, Violette S, Gonçalvès J, Ledoux E, Guyomard Y, Guillocheau F, et al. Long-term hydrodynamic response induced by past climatic and geomorphologic forcing: the case of the Paris basin, France. Phys Chem Earth, Parts A/B/C 2007;32:368–78. https://doi.org/10.1016/j.pce.2006.02.053.
[83] Ranchou-Peyruse M, Guignard M, Casteran F, Abadie M, Defois C, Peyret P, et al. Microbial diversity under the influence of natural gas storage in a deep aquifer. Front Microbiol 2021;12. https://doi.org/10.3389/fmicb.2021.688929.